

Nonlinear Aeroelasticity of a Very Flexible Blended-Wing-Body Aircraft

Weihua Su* and Carlos E. S. Cesnik†

University of Michigan, Ann Arbor, Michigan 48109-2140

DOI: 10.2514/1.47317

This paper presents a study on the coupled aeroelastic/flight dynamic stability and gust response of a blended-wing-body aircraft that derives from the U.S. Air Force's High Lift-Over-Drag Active (HiLDA) wing experimental model. An effective method is used to model very flexible blended-wing-body vehicles based on a low-order aeroelastic formulation that is capable of capturing the important structural nonlinear effects and couplings with the flight dynamic degrees of freedom. A nonlinear strain-based beam finite element formulation is used. Finite state unsteady subsonic aerodynamic loads are coupled to all lifting surfaces, including the flexible body. Based on the proposed model, aeroelastic stability is studied and compared with the flutter results with all or partial rigid-body degrees of freedom constrained. The applicability of wind-tunnel aeroelastic results (where the rigid-body motion is limited) is discussed in view of the free-flight conditions (with all 6 rigid-body degrees of freedom). Furthermore, effects of structural and aerodynamic nonlinearities as well as wing bending/torsion rigidity coupling on the aircraft characteristics are also discussed in this paper.

Nomenclature

\bar{A}	= system matrix of the linearized system
$A(s)$	= beam cross-sectional area
a_0	= local aerodynamic frame, with a_{0y} axis aligned with zero lift line of airfoil
a_1	= local aerodynamic frame, with a_{1y} axis aligned with airfoil motion velocity
B	= body reference frame
B_F, B_M	= influence matrices for the distributed forces and moments
b	= semichord of airfoil, m
b	= positions and orientations of the B frame, as time integral of β
b_n	= expansion coefficients for the inflow velocity
$C_{FF}, C_{FB}, C_{BF}, C_{BB}$	= components of the generalized damping matrix
$\bar{C}_{FF}, \bar{C}_{FB}, \bar{C}_{BF}, \bar{C}_{BB}$	= components of the generalized damping matrix of the linearized system
C^{Ba_1}	= rotation matrix from the a_1 frame to the B frame
C^{GB}	= rotation matrix from the B frame to the G frame
c_i, g_i	= coefficients based upon geometry of the trailing-edge control surfaces ($i = 1, 2, 3, \dots$)
d	= distance of midchord in front of beam reference axis, m
E_1, E_2, E_3, E_4	= influence matrices in the inflow equations with airfoil motion variables
F_1, F_2, F_3	= influence matrices in the inflow equations with independent variables
$F^{\text{aero}}, M^{\text{aero}}$	= nodal aerodynamic forces and moments

$F^{\text{dist}}, F^{\text{pt}}$	= distributed and point forces
G	= global (inertial) reference frame
g	= gravity acceleration vector
H_{hb}	= matrix consisting of influence from Jacobian (J_{hb}) and the body angular velocity (ω_B)
h	= absolute positions and orientations of beam nodes
h_r	= relative positions and orientations of beam nodes, with respect to the B frame
I	= identity matrix
I_{ij}	= mass moment of inertia of the beam cross section about its shear center ($i, j = x, y, z$)
J	= Jacobian matrix
$\mathbb{K}(s)$	= matrix of strain components
K_{FF}, \bar{K}_{FF}	= components of the generalized stiffness matrix of the linearized system
$k(s), c(s)$	= beam cross-sectional stiffness and damping matrices
k_{22}, k_{33}, k_{23}	= torsion, out-of-plane bending, and coupled torsion/out-of-plane bending components of $k(s)$
$l_{\text{mc}}, m_{\text{mc}}, d_{\text{mc}}$	= aerodynamic loads on an airfoil about its midchord
$l_{\text{ra}}, m_{\text{ra}}, d_{\text{ra}}$	= aerodynamic loads on an airfoil about beam reference axis
M, C, K	= discrete mass, damping, and stiffness matrices of the whole system
$M(s)$	= beam cross-sectional inertia matrix
M_e, C_e, K_e	= element mass, damping, and stiffness matrices
$M_{FF}, M_{FB}, M_{BF}, M_{BB}$	= components of the generalized mass matrix of the linearized system
$\bar{M}_{FF}, \bar{M}_{FB}, \bar{M}_{BF}, \bar{M}_{BB}$	= components of the generalized mass matrix of the linearized system
$M^{\text{dist}}, M^{\text{pt}}$	= distributed and point moments
m	= mass per unit length, kg/m
N	= influence matrix for the gravity force
\mathbb{N}	= number of inflow states
P_B	= inertial position of the B frame, resolved in the G frame
p_a	= position of an arbitrary point a with respect to the G frame
p_B, θ_B	= position and orientation of the B frame, as time integral of v_B and ω_B
p_w	= position of the w frame with respect to the B frame

Presented as Paper 2009-2402 at the 50th AIAA/ASME/ASCE/AHS/ASC Structures, Structural Dynamics, and Materials Conference, Palm Springs, CA, 4–7 May 2009; received 22 September 2009; revision received 25 June 2010; accepted for publication 29 June 2010. Copyright © 2010 by Weihua Su and Carlos E. S. Cesnik. Published by the American Institute of Aeronautics and Astronautics, Inc., with permission. Copies of this paper may be made for personal or internal use, on condition that the copier pay the \$10.00 per-copy fee to the Copyright Clearance Center, Inc., 222 Rosewood Drive, Danvers, MA 01923; include the code 0021-8669/10 and \$10.00 in correspondence with the CCC.

*Postdoctoral Research Fellow, Department of Aerospace Engineering; suw@umich.edu. Senior Member AIAA.

†Professor, Department of Aerospace Engineering; cesnik@umich.edu. Associate Fellow AIAA.

Q_1, Q_2	=	matrices of the state-space system equations
q	=	independent variables of the equations of motion
R_B, R_F	=	rigid-body and flexible components of the generalized load vector
$R_B^{\text{aero}}, R_F^{\text{aero}}$	=	rigid-body and flexible components of the generalized aerodynamic loads
$R_B^{\text{grav}}, R_F^{\text{grav}}$	=	rigid-body and flexible components of the generalized gravity force
r_x, r_y, r_z	=	position of the cross-sectional mass center in the w frame
s	=	beam curvilinear coordinate, m
v_B, ω_B	=	linear and angular velocities of the B frame, resolved in the B frame itself
$W^{\text{ext}}, W^{\text{int}}$	=	external and internal virtual work
w	=	local beam reference frame defined at each node along beam reference line
x	=	state variables
x, y, z	=	position of an arbitrary point a in the corresponding local w frame, m
\dot{y}, \dot{z}	=	airfoil translational velocity components resolved in the a_0 frame, m/s
$\dot{\alpha}$	=	airfoil angular velocity about the a_{0x} axis, rad/s
β	=	body velocities, with translational and angular components, resolved in the B frame
δ	=	trailing-edge control surface deflection, rad
ε	=	elastic strain vector
$\varepsilon_x, \kappa_x,$ κ_y, κ_z	=	element strains corresponding to extension, twist, out-of-plane, and in-plane bending
ε^0	=	initial (prescribed) elastic strain vector
ζ	=	quaternions defining the orientation of the B frame
η	=	stiffness-proportional damping coefficient
θ	=	rotations of beam nodes, rad
λ	=	inflow states, m/s
λ_0	=	inflow velocities, m/s
ρ	=	wing material density, kg/m ³
ρ_∞	=	air density, kg/m ³
σ	=	tuning parameter that determines the torsion/out-of-plane bending stiffness coupling
χ_0	=	nonlinear equilibrium state
$\Omega_\zeta(\beta)$	=	coefficient matrix of the quaternion equations, a function of body angular velocities

Subscripts

B	=	reference to the B frame
BB, BF	=	components of a matrix with respect to body/flexible differential equations of motion
e	=	element
F	=	reference to the flexible degrees of freedom
FB, FF	=	components of a matrix with respect to flexible/body differential equations of motion
hb	=	h vector with respect to the motion of the B frame
$h\varepsilon$	=	h vector with respect to the strain ε
pb	=	nodal position with respect to the motion of the B frame
$p\varepsilon$	=	nodal position with respect to the strain ε
θb	=	nodal rotation with respect to the motion of the B frame
$\theta\varepsilon$	=	nodal rotation with respect to the strain ε

I. Introduction

HIGH-ALTITUDE long-endurance (HALE) vehicles feature wings with high-aspect-ratio. These long and slender wings, by their inherent nature, can maximize lift-over-drag ratio. On the other hand, these wings may undergo large deformations during normal operating loads, exhibiting geometrically nonlinear behavior. Van

Schoor et al. [1] studied aeroelastic characteristics and control of highly flexible aircraft. They used linearized modes including rigid-body modes to predict the stability of the aircraft under different flight conditions. Their results indicated that unsteady aerodynamics and flexibility of the aircraft should be considered so as to correctly model the dynamic system. Patil et al. [2] studied the aeroelasticity and flight dynamics of HALE aircraft. They concluded that the large wing deformations due to the high-aspect-ratio structure may change the aerodynamic load distribution, compared to the initial shape, which may result in significant changes to the aeroelastic and flight dynamic behaviors of the wings and the overall aircraft. Therefore, the analysis results obtained through a linear analysis based on the undeformed shape may not be valid in this case, since those effects can only be obtained from a nonlinear analysis. A possible approximation to account for the geometric nonlinearity is to determine a nonlinear steady state, about which a linear dynamic analysis could be conducted. This breaks up, however, when the dynamic motion itself is nonlinear. In a parallel effort, Dreila [3] modeled a complete flexible aircraft as an assemblage of nonlinear beams. In his work, the aerodynamic model was a compressible vortex/source-lattice with wind-aligned trailing vorticity and Prandtl–Glauert compressibility correction. The nonlinear equation was solved using a full Newton method. Through simplifications of the model, the computational size was reduced for iterative preliminary designs. Shearer and Cesnik [4] also studied the nonlinear flight dynamics of very flexible aircraft. The nonlinear flight dynamic responses were governed by the coupled equations of the 6-DOF rigid-body motions and the nonlinear aeroelastic equations. They compared three sets of solutions: rigid, linearized, and fully nonlinear models, highlighting the importance of using the latter to properly model the very flexible vehicle motions. Su and Cesnik [5] studied the nonlinear dynamic response of a highly flexible flying-wing configuration. An asymmetric distributed gust model was applied to the time-domain simulations to study the nonlinear behaviors of the flying-wing configuration under such perturbations. Bilinear torsional stiffness changes due to wrinkling of the skin were addressed as well. Common to all those studies is the fact that the coupled effects between the vehicle flexibility and flight dynamics must be properly accounted for in a nonlinear aeroelastic formulation.

For the last several years, the U.S. Air Force has been working on new platform concepts for intelligence, surveillance, and reconnaissance missions, called sensorcraft. These are large HALE aircraft, with wing span of approximately 60 m. Three basic vehicle concepts have been considered: blended-wing-body, single-wing, and joined-wing configurations [6]. Among the sensorcraft concepts, this paper will focus on the blended-wing-body configuration. As an example of studies on this configuration, Beran et al. [7] performed static nonlinear aeroelastic analyses of a blended-wing-body. They used a high-fidelity computational tool to assess the contributions of aerodynamic nonlinearities to the transonic air loads sustained by a blended-wing-body with different static aeroelastic deflections. The structural deflections prescribed in the nonlinear analyses were obtained from a linear methodology. On the experimental side, a wind-tunnel model [8] was recently created by Northrop Grumman, under the Air Force's High Lift-Over-Drag Active (HiLDA) wing program to study the aeroelastic characteristics of blended-wing-body for a potential sensorcraft concept. In the report, a very lightly damped pure fore-aft bending mode was observed in the wind-tunnel test, which was not correctly modeled in their aeroelastic analysis tool, however. They suggested that this phenomena should be analytically explored further to fully characterize and understand the flexible wing fore-aft mode behavior [8]. The target model used in this paper is based on the HiLDA wind-tunnel model.

As pointed out in the literature (e.g., [2,4,5,9]), the coupling between the low-frequency rigid-body motions of the very flexible vehicle and its high-aspect-ratio, low-bending-frequency wings is very important. The natural frequencies of the wings are in the same range of the rigid-body ones, and they cannot be separated. Such proximity may lead to direct excitation of wing aeroelastic response due to rigid-body motions and vice versa. This can result in a dynamic instability known as body-freedom flutter [10]. This paper

focuses on the study of that aeroelastic instability, but in a nonlinear sense, where the instability boundary is dependent on the trim state and the size of the disturbance can drive a stable blended-wing-body aircraft to flutter.

II. Theoretical Formulation

Because of the interaction between flight dynamics and aeroelastic response, the formulation includes six rigid-body and multiple flexible degrees of freedom. The structural members are allowed fully coupled three-dimensional bending, twisting, and extensional deformations. Control surfaces are included for maneuver studies. A finite state unsteady aerodynamic model is integrated into the system equations. The model allows for a relatively low-order set of nonlinear equations that can be put into state-space form to facilitate stability analysis and control design. This formulation is implemented in MATLAB and is called the University of Michigan's Nonlinear Aeroelastic Simulation Toolbox (UM/NAST). An overview of the formulation implemented in UM/NAST is described below.

A. Fundamental Descriptions

As shown in Fig. 1, a global (inertial) frame G is defined, which is fixed on the ground. A body frame B is built in the global frame to describe the vehicle position and orientation, with B_x pointing to the right wing, B_y pointing forward, and B_z being the cross product of B_x and B_y . The position and orientation b and the time derivatives \dot{b} and \ddot{b} of the B frame can be defined as

$$b = \begin{Bmatrix} p_B \\ \theta_B \end{Bmatrix} \quad \dot{b} = \beta = \begin{Bmatrix} \dot{p}_B \\ \dot{\theta}_B \end{Bmatrix} = \begin{Bmatrix} v_B \\ \omega_B \end{Bmatrix} \quad (1)$$

$$\ddot{b} = \dot{\beta} = \begin{Bmatrix} \ddot{p}_B \\ \ddot{\theta}_B \end{Bmatrix} = \begin{Bmatrix} \dot{v}_B \\ \dot{\omega}_B \end{Bmatrix}$$

where p_B and θ_B are body position and orientation, both resolved in the body frame B . Note that the origin of the body frame is arbitrary in the vehicle and it does not have to be the location of the vehicle's center of gravity.

As described in Fig. 2, a local beam frame w is built within the body frame, which is used to define the position and orientation of each node along the beam reference line. Vectors w_x , w_y , and w_z are bases of the beam frame, whose directions are pointing along the beam reference axis, toward the leading edge, and normal to the beam surface, respectively, resolved in the body frame.

To model the elastic deformation of slender beams, a nonlinear beam element was developed [11,12]. Each of the elements has three nodes and four local strain degrees of freedom: extension, twist, and two bending strains of the beam reference line.

The positions and orientations of each node along the beam are defined by a vector consisting of 12 components, denoted as

$$h(s)^T = \{ (p_B + p_w(s))^T, w_x(s)^T, w_y(s)^T, w_z(s)^T \} \quad (2)$$

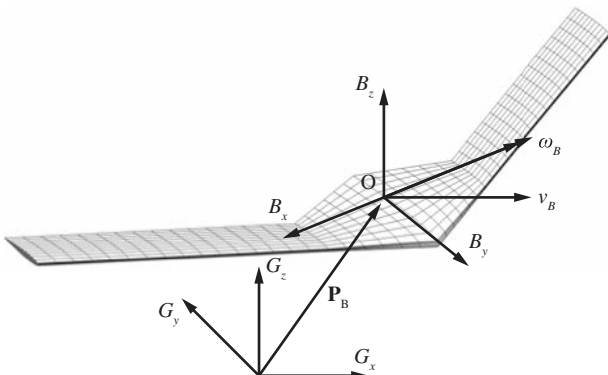


Fig. 1 Global and body reference frames.

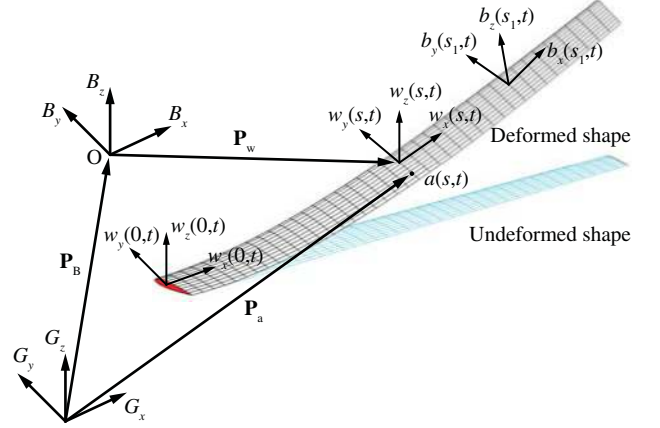


Fig. 2 Flexible lifting-surface frames and the body frame (for flight dynamics of the vehicle).

where p_w is the position of the w frame resolved in the body frame. In some cases, the nodal position and orientation information within the body frame is also necessary, defined as

$$h_r(s)^T = \{ p_w(s)^T, w_x(s)^T, w_y(s)^T, w_z(s)^T \} \quad (3)$$

It is easy to see that h_r is the displacement vector due to wing deformations, while h differs from h_r with the position of the body reference frame p_B .

With the elastic and rigid-body degrees of freedom defined, the complete independent set of variables of the strain-based formulation is

$$q = \begin{Bmatrix} \varepsilon \\ b \end{Bmatrix} = \begin{Bmatrix} \varepsilon \\ p_B \end{Bmatrix} \quad \dot{q} = \begin{Bmatrix} \dot{\varepsilon} \\ \dot{\beta} \end{Bmatrix} = \begin{Bmatrix} \dot{\varepsilon} \\ v_B \end{Bmatrix} \quad (4)$$

$$\ddot{q} = \begin{Bmatrix} \ddot{\varepsilon} \\ \ddot{\beta} \end{Bmatrix} = \begin{Bmatrix} \ddot{\varepsilon} \\ \dot{\omega}_B \end{Bmatrix}$$

The derivatives and variations of dependent variables h and h_r are related with those of the independent ones as

$$\delta h = J_{he} \delta \varepsilon + J_{hb} \delta b \quad \delta h_r = J_{he} \delta \varepsilon \quad dh = J_{he} d\varepsilon + J_{hb} db$$

$$dh_r = J_{he} d\varepsilon \quad \dot{h} = J_{he} \dot{\varepsilon} + J_{hb} \dot{\beta} = J_{he} \dot{\varepsilon} + J_{hb} \beta \quad \dot{h}_r = J_{he} \dot{\varepsilon}$$

$$\ddot{h} = J_{he} \ddot{\varepsilon} + \dot{J}_{he} \dot{\varepsilon} + J_{hb} \dot{\beta} + \dot{J}_{hb} \beta \quad \ddot{h}_r = J_{he} \ddot{\varepsilon} + \dot{J}_{he} \dot{\varepsilon} \quad (5)$$

where

$$J_{he} = \frac{\partial h}{\partial \varepsilon} \quad J_{hb} = \frac{\partial h}{\partial b} \quad (6)$$

are transformation Jacobians obtained from kinematics [4,12,13].

B. Elastic Equations of Motion

The elastic equations of motion are derived by following the principle of virtual work. The virtual work of an elastic wing consists of the contributions of inertia forces, internal strains and strain rates, and external loads. The contribution of each virtual work is derived separately and then summed at the end to represent the total virtual work of the complete vehicle.

1. Inertias

The virtual work due to the inertia of the elastic members is derived starting from the position of an arbitrary point a within the airfoil. As shown in Fig. 2, the position is given as

$$p_a = p_B + p_w + xw_x + yw_y + zw_z \quad (7)$$

where (x, y, z) is the position of the point within the local beam frame w . The infinitesimal virtual work applied on a unit volume is

$$\delta W_a = \delta \mathbf{p}_a \cdot (-\mathbf{a}_a \rho \, dA \, ds) \quad (8)$$

where

$$\mathbf{a}_a = \frac{d^2 \mathbf{p}_a}{dt^2} \quad (9)$$

The virtual work done by the inertia force along the beam coordinate s can be obtained by integrating Eq. (8) over each cross section, which yields

$$\begin{aligned} \delta W^{\text{int}}(s) = & -\delta h^T(s) \left(M(s) \begin{Bmatrix} \ddot{p}_w(s) \\ \ddot{w}_x(s) \\ \ddot{w}_y(s) \\ \ddot{w}_z(s) \end{Bmatrix} \right) + M(s) \begin{Bmatrix} I \tilde{p}_w^T(s) \\ 0 \tilde{w}_x^T(s) \\ 0 \tilde{w}_y^T(s) \\ 0 \tilde{w}_z^T(s) \end{Bmatrix} \dot{\beta} \\ & + M(s) \begin{bmatrix} \tilde{\omega}_B & 0 & 0 & 0 \\ 0 & \tilde{\omega}_B & 0 & 0 \\ 0 & 0 & \tilde{\omega}_B & 0 \\ 0 & 0 & 0 & \tilde{\omega}_B \end{bmatrix} \begin{bmatrix} I \tilde{p}_w^T(s) \\ 0 \tilde{w}_x^T(s) \\ 0 \tilde{w}_y^T(s) \\ 0 \tilde{w}_z^T(s) \end{bmatrix} \beta \\ & + 2M(s) \begin{bmatrix} 0 \\ 0 \\ 0 \\ 0 \end{bmatrix} \begin{bmatrix} \dot{\tilde{p}}_w^T(s) \\ \dot{\tilde{w}}_x^T(s) \\ \dot{\tilde{w}}_y^T(s) \\ \dot{\tilde{w}}_z^T(s) \end{bmatrix} \beta \end{aligned} \quad (10)$$

with

$$\begin{aligned} M(s) = & \int_{A(s)} \rho \begin{bmatrix} 1 & x & y & z \\ x & x^2 & xy & xz \\ y & yx & y^2 & yz \\ z & zx & zy & z^2 \end{bmatrix} dA \\ = & \begin{bmatrix} m & mr_x & mr_y & mr_z \\ mr_x & \frac{1}{2}(I_{yy} + I_{zz} - I_{xx}) & I_{xy} & I_{xz} \\ mr_y & I_{yx} & \frac{1}{2}(I_{zz} + I_{xx} - I_{yy}) & I_{yz} \\ mr_z & I_{zx} & I_{zy} & \frac{1}{2}(I_{xx} + I_{yy} - I_{zz}) \end{bmatrix} \end{aligned} \quad (11)$$

$M(s)$ is the cross-sectional inertial matrix, $A(s)$ is the cross-sectional area, m is the mass per unit span at each cross section, (r_x, r_y, r_z) is the position of the cross-sectional mass center in the w frame, and I_{ij} are the cross-sectional mass moments of inertia about the reference axis (shear center in the beam cross section). Note that the operator (\cdot) is defined for a 3 by 1 vector \mathbf{v} as

$$[\dot{\mathbf{v}}] \equiv \begin{bmatrix} 0 & -v_3 & v_2 \\ v_3 & 0 & -v_1 \\ -v_2 & v_1 & 0 \end{bmatrix} \quad (12)$$

In Eq. (10), $\{\dot{\tilde{p}}_w(s)^T \ \dot{\tilde{w}}_x(s)^T \ \dot{\tilde{w}}_y(s)^T \ \dot{\tilde{w}}_z(s)^T\}^T$ is the second time derivative of $h_r(s)$ given in Eq. (3). It can be written in terms of the second time derivative of the independent variables using Eq. (5). In addition, the following relations are defined:

$$\begin{aligned} J_{hb} \equiv & \begin{bmatrix} I \tilde{p}_w^T(s) \\ 0 \tilde{w}_x^T(s) \\ 0 \tilde{w}_y^T(s) \\ 0 \tilde{w}_z^T(s) \end{bmatrix} & \dot{J}_{hb} \equiv & \begin{bmatrix} 0 \dot{\tilde{p}}_w^T(s) \\ 0 \dot{\tilde{w}}_x^T(s) \\ 0 \dot{\tilde{w}}_y^T(s) \\ 0 \dot{\tilde{w}}_z^T(s) \end{bmatrix} \\ H_{hb} \equiv & \begin{bmatrix} \tilde{\omega}_B & 0 & 0 & 0 \\ 0 & \tilde{\omega}_B & 0 & 0 \\ 0 & 0 & \tilde{\omega}_B & 0 \\ 0 & 0 & 0 & \tilde{\omega}_B \end{bmatrix} & & \begin{bmatrix} I \tilde{p}_w^T(s) \\ 0 \tilde{w}_x^T(s) \\ 0 \tilde{w}_y^T(s) \\ 0 \tilde{w}_z^T(s) \end{bmatrix} \end{aligned} \quad (13)$$

With the above definitions, Eq. (10) can be simplified to

$$\begin{aligned} \delta W^{\text{int}}(s) = & -\{\delta \varepsilon^T(s) \ \delta b^T\} \left(\begin{bmatrix} J_{he}^T M(s) J_{he} & J_{he}^T M(s) J_{hb} \\ J_{hb}^T M(s) J_{he} & J_{hb}^T M(s) J_{hb} \end{bmatrix} \begin{Bmatrix} \ddot{\varepsilon}(s) \\ \dot{\beta} \end{Bmatrix} \right) \\ & + \begin{bmatrix} J_{he}^T M(s) \dot{J}_{he} & 0 \\ J_{hb}^T M(s) \dot{J}_{he} & 0 \end{bmatrix} \begin{Bmatrix} \dot{\varepsilon}(s) \\ \beta \end{Bmatrix} + \begin{bmatrix} 0 & J_{he}^T M(s) H_{hb} \\ 0 & J_{hb}^T M(s) H_{hb} \end{bmatrix} \begin{Bmatrix} \dot{\varepsilon}(s) \\ \beta \end{Bmatrix} \\ & + \begin{bmatrix} 0 & 2J_{he}^T M(s) \dot{J}_{hb} \\ 0 & 2J_{hb}^T M(s) \dot{J}_{hb} \end{bmatrix} \begin{Bmatrix} \dot{\varepsilon}(s) \\ \beta \end{Bmatrix} \end{aligned} \quad (14)$$

2. Internal Strain and Strain Rate

The virtual work due to the internal strain is

$$\delta W^{\text{int}}(s) = -\delta \varepsilon(s)^T k(s) (\varepsilon(s) - \varepsilon^0(s)) \quad (15)$$

where $k(s)$ is the cross-sectional stiffness matrix, and $\varepsilon^0(s)$ is the initial strain upon the beam initialization.

Internal damping is added to the formulation to better model the actual behavior of the structure. A stiffness-proportional damping is used in the current formulation, given by

$$c(s) = \eta k(s) \quad (16)$$

Thus, the virtual work due to the strain rate is

$$\delta W^{\text{int}}(s) = -\delta \varepsilon(s)^T c(s) \dot{\varepsilon}(s) \quad (17)$$

3. Internal Virtual Work on Element

To obtain the total internal virtual work on each element, one needs to summate Eqs. (14), (15), and (17) and then to integrate the summation over the length of the element. In practice, the integration is performed numerically.

As mentioned before, a three-node element is used in the current implementation. It is assumed that the strain over each element is constant. Some of the properties, such as inertias and displacements, are assumed to vary linearly between the three nodes of each element. However, the cross-sectional stiffness $k(s)$ and damping $c(s)$ are evaluated at the middle of each element and are assumed to be constant over the length of the element. With these assumptions, the internal virtual work of an element can be written as

$$\begin{aligned} \delta W_e^{\text{int}} = & -\{\delta \varepsilon_e^T \ \delta b^T\} \left(\begin{bmatrix} J_{he}^T M_e J_{he} & J_{he}^T M_e J_{hb} \\ J_{hb}^T M_e J_{he} & J_{hb}^T M_e J_{hb} \end{bmatrix} \begin{Bmatrix} \ddot{\varepsilon}_e \\ \dot{\beta} \end{Bmatrix} \right) \\ & + \begin{bmatrix} J_{he}^T M_e \dot{J}_{he} & 0 \\ J_{hb}^T M_e \dot{J}_{he} & 0 \end{bmatrix} \begin{Bmatrix} \dot{\varepsilon}_e \\ \beta \end{Bmatrix} + \begin{bmatrix} 0 & J_{he}^T M_e H_{hb} \\ 0 & J_{hb}^T M_e H_{hb} \end{bmatrix} \begin{Bmatrix} \dot{\varepsilon}_e \\ \beta \end{Bmatrix} \\ & + \begin{bmatrix} 0 & 2J_{he}^T M_e \dot{J}_{hb} \\ 0 & 2J_{hb}^T M_e \dot{J}_{hb} \end{bmatrix} \begin{Bmatrix} \dot{\varepsilon}_e \\ \beta \end{Bmatrix} + \begin{bmatrix} C_e & 0 \\ 0 & 0 \end{bmatrix} \begin{Bmatrix} \dot{\varepsilon}_e \\ \beta \end{Bmatrix} \\ & + \begin{bmatrix} K_e & 0 \\ 0 & 0 \end{bmatrix} \begin{Bmatrix} \varepsilon_e \\ b \end{Bmatrix} - \begin{bmatrix} K_e \varepsilon_e^0 \\ 0 \end{bmatrix} \end{aligned} \quad (18)$$

where

$$\begin{aligned} K_e = & k \Delta s & C_e = & c \Delta s \\ M_e = & \frac{1}{2} \Delta s \begin{bmatrix} \frac{1}{4} M_1 + \frac{1}{12} M_2 & \frac{1}{12} M_1 + \frac{1}{12} M_2 & 0 \\ \frac{1}{12} M_1 + \frac{1}{12} M_2 & \frac{1}{12} M_1 + \frac{1}{2} M_2 + \frac{1}{12} M_3 & \frac{1}{12} M_2 + \frac{1}{12} M_3 \\ 0 & \frac{1}{12} M_2 + \frac{1}{12} M_3 & \frac{1}{12} M_2 + \frac{1}{4} M_3 \end{bmatrix} \end{aligned} \quad (19)$$

ε_e in Eq. (18) is the element strain, Δs is the initial element length, K_e is the element stiffness matrix, C_e is the element damping matrix, M_e is the element inertia matrix, and M_i are the cross-sectional inertia matrices at each node of an element.

4. External Virtual Work

In general, the external virtual work applied on a differential volume can be written as

$$\delta W^{\text{ext}} = \int_V \delta \mathbf{u}(x, y, z) \cdot \mathbf{f}(x, y, z) dV \quad (20)$$

where $\mathbf{f}(x, y, z)$ represents generalized forces acting on the differential volume, which may include gravity forces, external distributed forces and moments, external point forces and moments, etc., and $\delta \mathbf{u}(x, y, z)$ is the corresponding virtual displacement. When beam cross-sectional properties are known, the integration of Eq. (20) over the volume is simplified to the integration along the beam coordinate s . The detailed derivation of the external virtual work is presented in [12].

5. Elastic Equations of Motion

The total virtual work on the system is obtained by summing up all elements' internal and external work:

$$\begin{aligned} \delta W &= \sum (\delta W_e^{\text{int}} + \delta W_e^{\text{ext}}) \\ &= \{ \delta \varepsilon^T \quad \delta b^T \} \left(- \begin{bmatrix} J_{he}^T M J_{he} & J_{he}^T M J_{hb} \\ J_{hb}^T M J_{he} & J_{hb}^T M J_{hb} \end{bmatrix} \begin{Bmatrix} \ddot{\varepsilon} \\ \dot{\beta} \end{Bmatrix} \right. \\ &\quad - \begin{bmatrix} J_{he}^T M \dot{J}_{he} & 0 \\ J_{hb}^T M \dot{J}_{he} & 0 \end{bmatrix} \begin{Bmatrix} \dot{\varepsilon} \\ \beta \end{Bmatrix} - \begin{bmatrix} 0 & J_{he}^T M H_{hb} \\ 0 & J_{hb}^T M H_{hb} \end{bmatrix} \begin{Bmatrix} \dot{\varepsilon} \\ \beta \end{Bmatrix} \\ &\quad - \begin{bmatrix} 0 & 2J_{he}^T M \dot{J}_{hb} \\ 0 & 2J_{hb}^T M \dot{J}_{hb} \end{bmatrix} \begin{Bmatrix} \dot{\varepsilon} \\ \beta \end{Bmatrix} - \begin{bmatrix} C & 0 \\ 0 & 0 \end{bmatrix} \begin{Bmatrix} \dot{\varepsilon} \\ \beta \end{Bmatrix} - \begin{bmatrix} K & 0 \\ 0 & 0 \end{bmatrix} \begin{Bmatrix} \varepsilon \\ b \end{Bmatrix} \\ &\quad + \begin{Bmatrix} K \varepsilon^0 \\ 0 \end{Bmatrix} - \begin{bmatrix} J_{he}^T \\ J_{hb}^T \end{bmatrix} N g + \begin{bmatrix} J_{pe}^T \\ J_{pb}^T \end{bmatrix} B_F F^{\text{dist}} + \begin{bmatrix} J_{\theta e}^T \\ J_{\theta b}^T \end{bmatrix} B_M M^{\text{dist}} \\ &\quad \left. + \begin{bmatrix} J_{pe}^T \\ J_{pb}^T \end{bmatrix} F^{\text{pt}} + \begin{bmatrix} J_{\theta e}^T \\ J_{\theta b}^T \end{bmatrix} M^{\text{pt}} \right) \quad (21) \end{aligned}$$

where N , B_F , and B_M are the influence matrices for the gravity force, distributed forces, and distributed moments, respectively, which come from the numerical integration. The equations of motion can be obtained by letting the total virtual work be zero. Since the variation $\{ \delta \varepsilon^T \quad \delta b^T \}$ is arbitrary, this leads to

$$\begin{aligned} &\begin{bmatrix} M_{FF} & M_{FB} \\ M_{BF} & M_{BB} \end{bmatrix} \begin{Bmatrix} \ddot{\varepsilon} \\ \dot{\beta} \end{Bmatrix} + \begin{bmatrix} C_{FF} & C_{FB} \\ C_{BF} & C_{BB} \end{bmatrix} \begin{Bmatrix} \dot{\varepsilon} \\ \beta \end{Bmatrix} + \begin{bmatrix} K_{FF} & 0 \\ 0 & 0 \end{bmatrix} \begin{Bmatrix} \varepsilon \\ b \end{Bmatrix} \\ &= \begin{Bmatrix} R_F \\ R_B \end{Bmatrix} \quad (22) \end{aligned}$$

where the generalized inertia, damping, and stiffness matrices are

$$\begin{aligned} M_{FF}(\varepsilon) &= J_{he}^T M J_{he} & M_{FB}(\varepsilon) &= J_{he}^T M J_{hb} \\ M_{BF}(\varepsilon) &= J_{hb}^T M J_{he} & M_{BB}(\varepsilon) &= J_{hb}^T M J_{hb} \\ C_{FF}(\varepsilon, \dot{\varepsilon}, \beta) &= C + J_{he}^T M \dot{J}_{he} \\ C_{FB}(\varepsilon, \dot{\varepsilon}, \beta) &= J_{he}^T M H_{hb} + 2J_{he}^T M \dot{J}_{hb} \\ C_{BF}(\varepsilon, \dot{\varepsilon}, \beta) &= J_{hb}^T M \dot{J}_{he} \\ C_{BB}(\varepsilon, \dot{\varepsilon}, \beta) &= J_{hb}^T M H_{hb} + 2J_{hb}^T M \dot{J}_{hb} \\ K_{FF} &= K \quad (23) \end{aligned}$$

and the generalized force vector is

$$\begin{aligned} \begin{Bmatrix} R_F \\ R_B \end{Bmatrix} &= \begin{Bmatrix} K_{FF} \varepsilon^0 \\ 0 \end{Bmatrix} - \begin{bmatrix} J_{he}^T \\ J_{hb}^T \end{bmatrix} N g + \begin{bmatrix} J_{pe}^T \\ J_{pb}^T \end{bmatrix} B_F F^{\text{dist}} \\ &\quad + \begin{bmatrix} J_{\theta e}^T \\ J_{\theta b}^T \end{bmatrix} B_M M^{\text{dist}} + \begin{bmatrix} J_{pe}^T \\ J_{pb}^T \end{bmatrix} F^{\text{pt}} + \begin{bmatrix} J_{\theta e}^T \\ J_{\theta b}^T \end{bmatrix} M^{\text{pt}} \quad (24) \end{aligned}$$

which involves the effects from initial strains ε^0 , gravity field g , distributed forces F^{dist} , distributed moments M^{dist} , point forces F^{pt} , and point moments M^{pt} . The aerodynamic forces and moments are considered as distributed loads.

C. Kinematics

As discussed in [12], the governing equation, which relates the dependent displacements to the independent strains, is

$$\frac{\partial h(s)}{\partial s} = \mathbb{K}(s)h(s) \quad (25)$$

with $\mathbb{K}(s)$ being a matrix function of the strains, i.e.,

$$\mathbb{K}(s) = \begin{bmatrix} 0 & 1 + \varepsilon_x(s) & 0 & 0 \\ 0 & 0 & \kappa_z(s) & -\kappa_y(s) \\ 0 & -\kappa_z(s) & 0 & \kappa_x(s) \\ 0 & \kappa_y(s) & -\kappa_x(s) & 0 \end{bmatrix} \quad (26)$$

Note that each entry in the above matrix is a 3 by 3 diagonal matrix. With the assumption that each element has a constant strain state, the solution of Eq. (25) is given by

$$h(s) = e^{\mathbb{K}(s-s_0)} h_0 = e^{G(s)} h_0 \quad (27)$$

where h_0 is the displacement of a fixed or prescribed root node of the beam (boundary conditions). The nodal displacements can then be recovered from the strain vector by marching Eq. (27) from the prescribed node to the tips of each beam member.

D. Unsteady Aerodynamics

The distributed loads, F^{dist} and M^{dist} in Eq. (24), are divided into aerodynamic loads and user-supplied loads. The unsteady aerodynamic loads used in the current study are based on the 2-D finite state inflow theory provided in [14]. The theory calculates aerodynamic loads on a thin-airfoil section undergoing large motions in an incompressible inviscid subsonic flow. The lift, moment, and drag of a thin 2-D airfoil section about its midchord are given by

$$\begin{aligned} l_{\text{mc}} &= \pi \rho_\infty b^2 (-\ddot{z} + \dot{y} \dot{\alpha} - d \ddot{\alpha}) + 2\pi \rho_\infty b \dot{y}^2 \left[-\frac{\dot{z}}{\dot{y}} + \left(\frac{1}{2} b - d \right) \frac{\dot{\alpha}}{\dot{y}} \right. \\ &\quad \left. - \frac{\lambda_0}{\dot{y}} \right] + 2\pi \rho_\infty b c_1 \dot{y}^2 \delta \\ m_{\text{mc}} &= \pi \rho_\infty b^2 \left(-\frac{1}{8} b^2 \ddot{\alpha} - \dot{y} \dot{z} - d \dot{y} \dot{\alpha} - \dot{y} \lambda_0 \right) + 2\pi \rho_\infty b^2 c_4 \dot{y}^2 \delta \\ d_{\text{mc}} &= -2\pi \rho_\infty b (\dot{z}^2 + d^2 \dot{\alpha}^2 + \lambda_0^2 + 2d\dot{z}\dot{\alpha} + 2\dot{z}\lambda_0 + 2d\dot{\alpha}\lambda_0) \\ &\quad - 2\pi \rho_\infty b \left[-c_1 \dot{y} \dot{z} \delta - (dc_1 + bg_1) \dot{y} \dot{\alpha} \delta - c_1 \dot{y} \lambda_0 \delta + \frac{1}{2} bg_1 \dot{z} \delta \right. \\ &\quad \left. + \left(\frac{1}{2} bdg_1 - \frac{1}{4} b^2 g_2 \right) \ddot{\alpha} \delta \right] \quad (28) \end{aligned}$$

where δ is the trailing-edge flap deflection angle, b is the semichord, and d is the distance of the midchord in front of the reference axis. The quantity $-\dot{z}/\dot{y}$ is the angle of attack that consists of the contribution from both the pitching angle and the unsteady plunging motion of the airfoil. (The different velocity components are shown in Fig. 3.) The coefficients c_i through g_i are based upon the geometry of trailing-edge flaps, and their expressions are provided in [14].

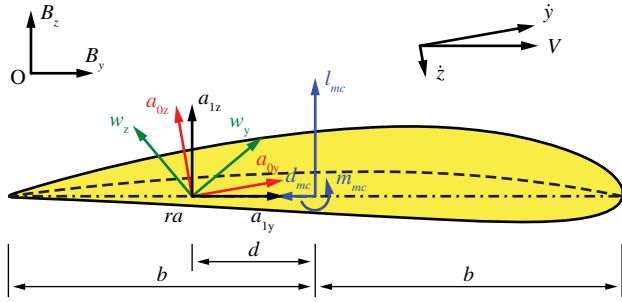


Fig. 3 Airfoil coordinate systems and velocity components.

The inflow velocity λ_0 is given by

$$\lambda_0 = \frac{1}{2} \sum_{n=1}^{\mathbb{N}} b_n \lambda_n \quad (29)$$

where λ_n represents the inflow states determined from

$$\dot{\lambda} = E_1 \lambda + E_2 \ddot{z} + E_3 \ddot{\alpha} + E_4 \dot{\alpha} \quad (30)$$

The coefficient matrices E_i are given in [14], and b_n are obtained by least-squares method [15]. Theoretically, λ_0 is an infinite summation. However, it can be approximated by letting \mathbb{N} be between 4 and 8. Equation (30) can be expressed in terms of the independent system variables by using the Jacobians as

$$\dot{\lambda} = F_1 \ddot{q} + F_2 \dot{q} + F_3 \lambda = F_1 \begin{Bmatrix} \ddot{\varepsilon} \\ \dot{\beta} \end{Bmatrix} + F_2 \begin{Bmatrix} \dot{\varepsilon} \\ \beta \end{Bmatrix} + F_3 \lambda \quad (31)$$

To transfer the loads from the midchord (as defined above) to the wing reference axis, one may use

$$l_{ra} = l_{mc} \quad m_{ra} = m_{mc} + d l_{mc} \quad d_{ra} = d_{mc} \quad (32)$$

Furthermore, the loads are rotated to the body reference frame, which yields

$$F^{\text{aero}} = C^{Ba_1} \begin{Bmatrix} 0 \\ d_{ra} \\ l_{ra} \end{Bmatrix} \quad M^{\text{aero}} = C^{Ba_1} \begin{Bmatrix} m_{ra} \\ 0 \\ 0 \end{Bmatrix} \quad (33)$$

where C^{Ba_1} is the transformation matrix from the local aerodynamic frame to the body frame. Note that Prandtl–Glauert compressibility correction is applied to this formulation, and the finite span corrections are also included in the force distribution and may come from a CFD solution of the problem or experimental data if available.

E. Coupled Nonlinear Aeroelastic and Flight Dynamic System Equations of Motion

The coupled nonlinear aeroelastic and flight dynamic system equations of motion are obtained by augmenting the equations of rigid-body motion and elastic deformations with the inflow equations, which can be represented as

$$\begin{bmatrix} M_{FF}(\varepsilon) & M_{FB}(\varepsilon) \\ M_{BF}(\varepsilon) & M_{BB}(\varepsilon) \end{bmatrix} \begin{Bmatrix} \ddot{\varepsilon} \\ \dot{\beta} \end{Bmatrix} + \begin{bmatrix} C_{FF}(\dot{\varepsilon}, \varepsilon, \beta) & C_{FB}(\dot{\varepsilon}, \varepsilon, \beta) \\ C_{BF}(\dot{\varepsilon}, \varepsilon, \beta) & C_{BB}(\dot{\varepsilon}, \varepsilon, \beta) \end{bmatrix} \begin{Bmatrix} \dot{\varepsilon} \\ \beta \end{Bmatrix} + \begin{bmatrix} K_{FF} & 0 \\ 0 & 0 \end{bmatrix} \begin{Bmatrix} \varepsilon \\ b \end{Bmatrix} = \begin{Bmatrix} R_F(\ddot{\varepsilon}, \dot{\varepsilon}, \varepsilon, \dot{\beta}, \beta, \lambda, \zeta) \\ R_B(\ddot{\varepsilon}, \dot{\varepsilon}, \varepsilon, \dot{\beta}, \beta, \lambda, \zeta) \end{Bmatrix} \\ \dot{\zeta} = -\frac{1}{2} \Omega_{\zeta}(\beta) \zeta \quad \dot{P}_B = [C^{GB}(\zeta) \quad 0] \beta \\ \dot{\lambda} = F_1 \begin{Bmatrix} \ddot{\varepsilon} \\ \dot{\beta} \end{Bmatrix} + F_2 \begin{Bmatrix} \dot{\varepsilon} \\ \beta \end{Bmatrix} + F_3 \lambda \quad (34)$$

where ζ is the quaternions describing the orientation of the body frame B , P_B is the inertial position of the B frame, and C^{GB} is the rotation matrix from the body frame to global frame G [4].

F. Linearization of the Nonlinear System Equations of Motion

The coupled nonlinear aeroelastic and flight dynamic system equations of motion are given by Eq. (34). Without loss of generality, the terms associated with the control surface deflection angles in the aerodynamic load formulation are not included from this point on, since the objective of this paper is to study the stability of the trimmed vehicle. The control surface deflections are only used to trim the vehicle before the stability analysis. Therefore, the load vector simplifies to contributions from aerodynamic and gravity loads only; i.e.,

$$\begin{Bmatrix} R_F(\ddot{\varepsilon}, \dot{\varepsilon}, \varepsilon, \dot{\beta}, \beta, \lambda, \zeta) \\ R_B(\ddot{\varepsilon}, \dot{\varepsilon}, \varepsilon, \dot{\beta}, \beta, \lambda, \zeta) \end{Bmatrix} = \begin{Bmatrix} R_F^{\text{aero}}(\ddot{\varepsilon}, \dot{\varepsilon}, \varepsilon, \dot{\beta}, \beta, \lambda) \\ R_B^{\text{aero}}(\ddot{\varepsilon}, \dot{\varepsilon}, \varepsilon, \dot{\beta}, \beta, \lambda) \end{Bmatrix} + \begin{Bmatrix} R_F^{\text{grav}}(\zeta) \\ R_B^{\text{grav}}(\zeta) \end{Bmatrix} \quad (35)$$

and

$$\begin{Bmatrix} R_F^{\text{aero}} \\ R_B^{\text{aero}} \end{Bmatrix} = \begin{bmatrix} J_{pe}^T \\ J_{pb}^T \end{bmatrix} B_F F^{\text{aero}} + \begin{bmatrix} J_{\theta\varepsilon}^T \\ J_{\theta\beta}^T \end{bmatrix} B_M M^{\text{aero}} \quad (36)$$

where F^{aero} and M^{aero} are the nodal aerodynamic loads. R_F^{aero} and R_B^{aero} are the flexible and rigid-body components of the generalized aerodynamic loads, respectively, and R_F^{grav} and R_B^{grav} are the flexible and rigid-body components of the generalized gravity force, respectively. The gravity force is transferred from the global frame G to the body frame B . The rotation matrix between the two frames (C^{GB}) is a function of quaternions ζ , according to Eq. (34).

Linearization is performed about a nonlinear equilibrium state, given by

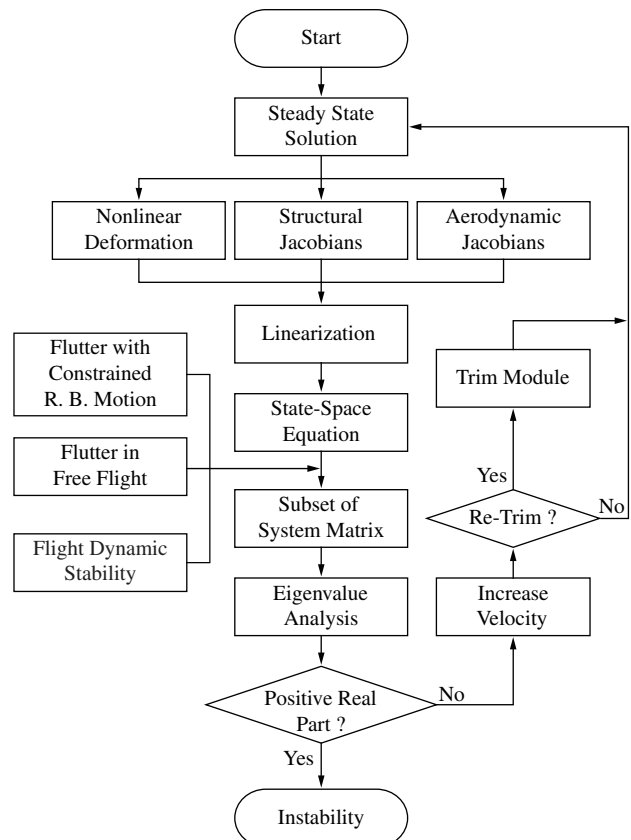


Fig. 4 Searching scheme for the stability boundary (R. B. denotes rigid body).

$$\chi_0^T = \{\dot{\varepsilon}_0^T, \dot{\beta}_0^T, \dot{\lambda}_0^T, \dot{\zeta}_0^T, P_{B0}^T\} \quad (37)$$

From that, the linearized system equations can be derived as

$$\begin{aligned} M_{FF}\ddot{\varepsilon} + M_{FB}\dot{\beta} + (C_{FF} + C_{FF/\dot{\varepsilon}_0}\dot{\varepsilon}_0 + C_{FB/\dot{\varepsilon}_0}\dot{\beta}_0)\dot{\varepsilon} \\ + (C_{FB} + C_{FF/\beta_0}\dot{\varepsilon}_0 + C_{FB/\beta_0}\dot{\beta}_0)\beta + K_{FF}\varepsilon = R_{F/\dot{\varepsilon}_0}^{\text{aero}}\ddot{\varepsilon} \\ + R_{F/\dot{\varepsilon}_0}^{\text{aero}}\dot{\varepsilon} + R_{F/\varepsilon_0}^{\text{aero}}\varepsilon + R_{F/\beta_0}^{\text{aero}}\dot{\beta} + R_{F/\beta_0}^{\text{aero}}\beta + R_{F/\lambda_0}^{\text{aero}}\lambda + R_{F/\zeta_0}^{\text{grav}}\zeta \\ M_{BF}\ddot{\varepsilon} + M_{BB}\dot{\beta} + (C_{BF} + C_{BF/\dot{\varepsilon}_0}\dot{\varepsilon}_0 + C_{BB/\dot{\varepsilon}_0}\dot{\beta}_0)\dot{\varepsilon} + (C_{BB} \\ + C_{BF/\beta_0}\dot{\varepsilon}_0 + C_{BB/\beta_0}\dot{\beta}_0)\beta = R_{B/\dot{\varepsilon}_0}^{\text{aero}}\ddot{\varepsilon} + R_{B/\dot{\varepsilon}_0}^{\text{aero}}\dot{\varepsilon} + R_{B/\varepsilon_0}^{\text{aero}}\varepsilon \\ + R_{B/\beta_0}^{\text{aero}}\dot{\beta} + R_{B/\beta_0}^{\text{aero}}\beta + R_{B/\lambda_0}^{\text{aero}}\lambda + R_{B/\zeta_0}^{\text{grav}}\zeta \\ \dot{\zeta} = -\frac{1}{2}\Omega_\zeta\zeta - \frac{1}{2}(\Omega_{\zeta/\beta_0}\beta)\zeta_0 \\ \dot{P}_B = [C^{GB} \ 0]\beta + [(C_{/50}^{GB}\zeta) \ 0]\beta_0 \\ \dot{\lambda} = F_1\left\{\begin{array}{c} \ddot{\varepsilon} \\ \dot{\beta} \end{array}\right\} + F_2\left\{\begin{array}{c} \dot{\varepsilon} \\ \beta \end{array}\right\} + F_3\lambda \end{aligned} \quad (38)$$

where $(\cdot)_{/z_0}$ denotes $\partial(\cdot)/\partial z|_{z_0}$, with z representing one of the χ_0 components.

To obtain the state-space form of these equations, the terms on the right-hand side of Eq. (38) are moved to the left, and the terms with the same variables are grouped together, yielding

$$\begin{aligned} (M_{FF} - R_{F/\dot{\varepsilon}_0}^{\text{aero}})\ddot{\varepsilon} + (M_{FB} - R_{F/\beta_0}^{\text{aero}})\dot{\beta} + (C_{FF} + C_{FF/\dot{\varepsilon}_0}\dot{\varepsilon}_0 \\ + C_{FB/\dot{\varepsilon}_0}\dot{\beta}_0 - R_{F/\dot{\varepsilon}_0}^{\text{aero}})\dot{\varepsilon} + (C_{FB} + C_{FF/\beta_0}\dot{\varepsilon}_0 + C_{FB/\beta_0}\dot{\beta}_0 \\ - R_{F/\beta_0}^{\text{aero}})\beta + (K_{FF} - R_{F/\varepsilon_0}^{\text{aero}})\varepsilon - R_{F/\lambda_0}^{\text{aero}}\lambda - R_{F/\zeta_0}^{\text{grav}}\zeta = 0 \\ (M_{BF} - R_{B/\dot{\varepsilon}_0}^{\text{aero}})\ddot{\varepsilon} + (M_{BB} - R_{B/\beta_0}^{\text{aero}})\dot{\beta} + (C_{BF} + C_{BF/\dot{\varepsilon}_0}\dot{\varepsilon}_0 \\ + C_{BB/\dot{\varepsilon}_0}\dot{\beta}_0 - R_{B/\dot{\varepsilon}_0}^{\text{aero}})\dot{\varepsilon} + (C_{BB} + C_{BF/\beta_0}\dot{\varepsilon}_0 + C_{BB/\beta_0}\dot{\beta}_0 \\ - R_{B/\beta_0}^{\text{aero}})\beta - R_{B/\lambda_0}^{\text{aero}}\lambda - R_{B/\zeta_0}^{\text{grav}}\zeta = 0 \\ \dot{\zeta} + \frac{1}{2}\Omega_\zeta\zeta + \frac{1}{2}(\Omega_{\zeta/\beta_0}\beta)\zeta_0 = 0 \\ \dot{P}_B - [C^{GB} \ 0]\beta - [(C_{/50}^{GB}\zeta) \ 0]\beta_0 = 0 \\ \dot{\lambda} - F_1\left\{\begin{array}{c} \ddot{\varepsilon} \\ \dot{\beta} \end{array}\right\} - F_2\left\{\begin{array}{c} \dot{\varepsilon} \\ \beta \end{array}\right\} - F_3\lambda = 0 \end{aligned} \quad (39)$$

According to Eq. (36), the derivatives of the generalized aerodynamic loads can be expanded, resulting in

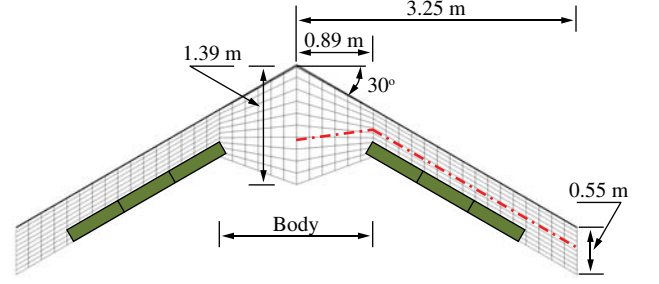


Fig. 5 Geometry of the blended-wing-body model.

$$\begin{aligned} \frac{\partial R_F^{\text{aero}}}{\partial \varepsilon} &= J_{pe}^T B_F \frac{\partial F^{\text{aero}}}{\partial \varepsilon} + J_{\theta e}^T B_M \frac{\partial M^{\text{aero}}}{\partial \varepsilon} \\ \frac{\partial R_F^{\text{aero}}}{\partial \beta} &= J_{pe}^T B_F \frac{\partial F^{\text{aero}}}{\partial \beta} + J_{\theta e}^T B_M \frac{\partial M^{\text{aero}}}{\partial \beta} \\ \frac{\partial R_F^{\text{aero}}}{\partial \dot{\varepsilon}} &= J_{pe}^T B_F \frac{\partial F^{\text{aero}}}{\partial \dot{\varepsilon}} + J_{\theta e}^T B_M \frac{\partial M^{\text{aero}}}{\partial \dot{\varepsilon}} \\ \frac{\partial R_F^{\text{aero}}}{\partial \beta} &= J_{pe}^T B_F \frac{\partial F^{\text{aero}}}{\partial \beta} + J_{\theta e}^T B_M \frac{\partial M^{\text{aero}}}{\partial \beta} \\ \frac{\partial R_F^{\text{aero}}}{\partial \varepsilon} &= J_{pe}^T B_F \frac{\partial F^{\text{aero}}}{\partial \varepsilon} + J_{\theta e}^T B_M \frac{\partial M^{\text{aero}}}{\partial \varepsilon} \\ \frac{\partial R_B^{\text{aero}}}{\partial \varepsilon} &= J_{pb}^T B_F \frac{\partial F^{\text{aero}}}{\partial \varepsilon} + J_{\theta b}^T B_M \frac{\partial M^{\text{aero}}}{\partial \varepsilon} \\ \frac{\partial R_B^{\text{aero}}}{\partial \beta} &= J_{pb}^T B_F \frac{\partial F^{\text{aero}}}{\partial \beta} + J_{\theta b}^T B_M \frac{\partial M^{\text{aero}}}{\partial \beta} \\ \frac{\partial R_B^{\text{aero}}}{\partial \dot{\varepsilon}} &= J_{pb}^T B_F \frac{\partial F^{\text{aero}}}{\partial \dot{\varepsilon}} + J_{\theta b}^T B_M \frac{\partial M^{\text{aero}}}{\partial \dot{\varepsilon}} \\ \frac{\partial R_B^{\text{aero}}}{\partial \beta} &= J_{pb}^T B_F \frac{\partial F^{\text{aero}}}{\partial \beta} + J_{\theta b}^T B_M \frac{\partial M^{\text{aero}}}{\partial \beta} \end{aligned} \quad (40)$$

Again, one should note that all the derivatives and matrices are evaluated at the equilibrium state χ_0 , and the notation is omitted from the equations from now on for simplicity. Using Eq. (40), Eq. (39) can be written as

$$\begin{aligned} \bar{M}_{FF}\ddot{\varepsilon} + \bar{M}_{FB}\dot{\beta} + \bar{C}_{FF}\dot{\varepsilon} + \bar{C}_{FB}\beta + \bar{K}_{FF}\varepsilon - R_{F/\lambda_0}^{\text{aero}}\lambda - R_{F/\zeta_0}^{\text{grav}}\zeta = 0 \\ \bar{M}_{BF}\ddot{\varepsilon} + \bar{M}_{BB}\dot{\beta} + \bar{C}_{BF}\dot{\varepsilon} + \bar{C}_{BB}\beta - R_{B/\lambda_0}^{\text{aero}}\lambda - R_{B/\zeta_0}^{\text{grav}}\zeta = 0 \\ \dot{\zeta} + \frac{1}{2}\Omega_\zeta\zeta + \frac{1}{2}(\Omega_{\zeta/\beta_0}\beta)\zeta_0 = 0 \\ \dot{P}_B - [C^{GB} \ 0]\beta - [(C_{/50}^{GB}\zeta) \ 0]\beta_0 = 0 \\ \dot{\lambda} - F_1\left\{\begin{array}{c} \ddot{\varepsilon} \\ \dot{\beta} \end{array}\right\} - F_2\left\{\begin{array}{c} \dot{\varepsilon} \\ \beta \end{array}\right\} - F_3\lambda = 0 \end{aligned} \quad (41)$$

where

Table 1 Properties of the body and wing members of the blended-wing-body model

	Body	Wing	Units
Ref axis location (root/tip) (from leading edge)	64.38%/45.60% chord	45.60%/45.60% chord	—
Center of gravity (root/tip) (from leading edge)	64.38%/45.60% chord	45.60%/45.60% chord	—
Extension stiffness	1.69×10^8	1.55×10^8	N
Out-of-plane bending stiffness	7.50×10^5	1.14×10^4	N · m ²
In-plane bending stiffness	3.50×10^7	1.30×10^5	N · m ²
Torsion stiffness	2.25×10^6	1.10×10^4	N · m ²
Mass per unit length	50.00	6.20	kg/m
Flat bending inertia per unit length	0.70	5.00×10^{-4}	kg · m
Edge bending inertia per unit length	22.00	4.63×10^{-3}	kg · m
Rotational inertia per unit length	4.50	5.08×10^{-3}	kg · m

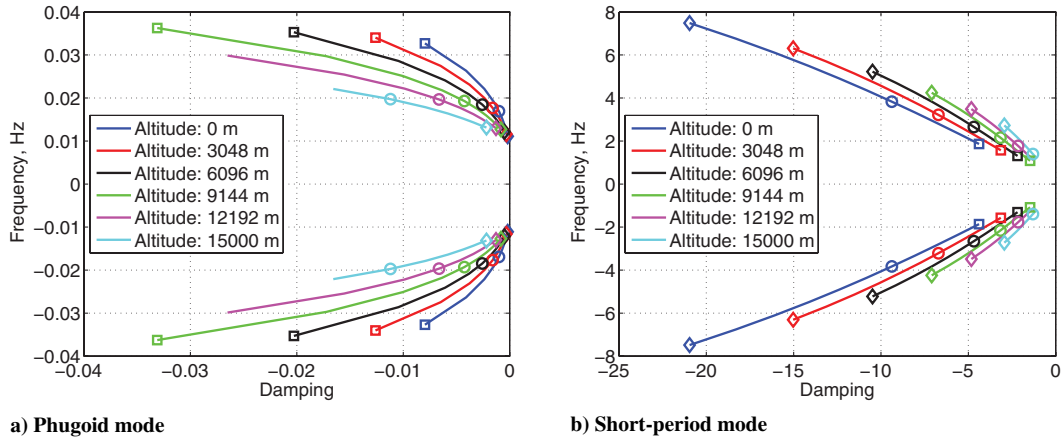


Fig. 6 Root locus of phugoid and short-period modes of the blended-wing-body configuration at different altitudes; speed from Mach 0.2 (square) to 0.7 (diamond).

$$\begin{aligned}
 \bar{M}_{FF} &= M_{FF} - J_{p\epsilon}^T B_F \frac{\partial F^{\text{aero}}}{\partial \ddot{\epsilon}} - J_{\theta\epsilon}^T B_M \frac{\partial M^{\text{aero}}}{\partial \ddot{\epsilon}} \\
 \bar{M}_{FB} &= M_{FB} - J_{p\epsilon}^T B_F \frac{\partial F^{\text{aero}}}{\partial \dot{\beta}} - J_{\theta\epsilon}^T B_M \frac{\partial M^{\text{aero}}}{\partial \dot{\beta}} \\
 \bar{C}_{FF} &= C_{FF} + \frac{\partial C_{FF}}{\partial \dot{\epsilon}} \dot{\epsilon}_0 + \frac{\partial C_{FB}}{\partial \dot{\epsilon}} \beta_0 - J_{p\epsilon}^T B_F \frac{\partial F^{\text{aero}}}{\partial \dot{\epsilon}} \\
 &\quad - J_{\theta\epsilon}^T B_M \frac{\partial M^{\text{aero}}}{\partial \dot{\epsilon}} \\
 \bar{C}_{FB} &= C_{FB} + \frac{\partial C_{FF}}{\partial \dot{\beta}} \dot{\epsilon}_0 + \frac{\partial C_{FB}}{\partial \dot{\beta}} \beta_0 - J_{p\epsilon}^T B_F \frac{\partial F^{\text{aero}}}{\partial \dot{\beta}} \\
 &\quad - J_{\theta\epsilon}^T B_M \frac{\partial M^{\text{aero}}}{\partial \dot{\beta}} \\
 \bar{K}_{FF} &= K_{FF} - J_{p\epsilon}^T B_F \frac{\partial F^{\text{aero}}}{\partial \epsilon} - J_{\theta\epsilon}^T B_M \frac{\partial M^{\text{aero}}}{\partial \epsilon}
 \end{aligned} \quad (42)$$

and

$$\begin{aligned}
 \bar{M}_{BF} &= M_{BF} - J_{pb}^T B_F \frac{\partial F^{\text{aero}}}{\partial \ddot{\epsilon}} - J_{\theta b}^T B_M \frac{\partial M^{\text{aero}}}{\partial \ddot{\epsilon}} \\
 \bar{M}_{BB} &= M_{BB} - J_{pb}^T B_F \frac{\partial F^{\text{aero}}}{\partial \dot{\beta}} - J_{\theta b}^T B_M \frac{\partial M^{\text{aero}}}{\partial \dot{\beta}} \\
 \bar{C}_{BF} &= C_{BF} + \frac{\partial C_{BF}}{\partial \dot{\epsilon}} \dot{\epsilon}_0 + \frac{\partial C_{BB}}{\partial \dot{\epsilon}} \beta_0 - J_{pb}^T B_F \frac{\partial F^{\text{aero}}}{\partial \dot{\epsilon}} \\
 &\quad - J_{\theta b}^T B_M \frac{\partial M^{\text{aero}}}{\partial \dot{\epsilon}} \\
 \bar{C}_{BB} &= C_{BB} + \frac{\partial C_{BF}}{\partial \dot{\beta}} \dot{\epsilon}_0 + \frac{\partial C_{BB}}{\partial \dot{\beta}} \beta_0 - J_{pb}^T B_F \frac{\partial F^{\text{aero}}}{\partial \dot{\beta}} \\
 &\quad - J_{\theta b}^T B_M \frac{\partial M^{\text{aero}}}{\partial \dot{\beta}}
 \end{aligned} \quad (43)$$

Table 2 Blended-wing-body fundamental modes and frequencies

No.	Mode	Frequency, Hz
1	First flatwise bending	3.3
2	First edgewise bending	10.9
3	Second flatwise bending	20.4
4	Third flatwise bending	55.6
5	Second edgewise bending	69.5
6	Fourth flatwise bending	82.0

Finally, Eq. (41) can be put into the state-space form:

$$\begin{aligned}
 &\{\dot{\epsilon}^T \quad \ddot{\epsilon}^T \quad \dot{\beta}^T \quad \zeta^T \quad \dot{P}_B^T \quad \lambda^T\}^T \\
 &= Q_1^{-1} Q_2 \{\epsilon^T \quad \dot{\epsilon}^T \quad \beta^T \quad \zeta^T \quad P_B^T \quad \lambda^T\}^T \\
 &= \bar{A} \{\epsilon^T \quad \dot{\epsilon}^T \quad \beta^T \quad \zeta^T \quad P_B^T \quad \lambda^T\}^T
 \end{aligned} \quad (44)$$

or

$$\dot{x} = \bar{A}x \quad (45)$$

where

$$x^T = \{\epsilon^T \quad \dot{\epsilon}^T \quad \beta^T \quad \zeta^T \quad P_B^T \quad \lambda^T\} \quad (46)$$

$$Q_1 = \begin{bmatrix} I & 0 & 0 & 0 & 0 & 0 \\ 0 & \bar{M}_{FF} & \bar{M}_{FB} & 0 & 0 & 0 \\ 0 & \bar{M}_{BF} & \bar{M}_{BB} & 0 & 0 & 0 \\ 0 & 0 & 0 & I & 0 & 0 \\ 0 & 0 & 0 & 0 & I & 0 \\ 0 & -F_{1F} & -F_{1B} & 0 & 0 & I \end{bmatrix}$$

$$Q_2 = \begin{bmatrix} 0 & I & 0 & 0 & 0 & 0 \\ -\bar{K}_{FF} & -\bar{C}_{FF} & -\bar{C}_{FB} & R_{F/\zeta_0}^{\text{grav}} & 0 & R_{F/\lambda_0}^{\text{aero}} \\ 0 & -\bar{C}_{BF} & -\bar{C}_{BB} & R_{B/\zeta_0}^{\text{grav}} & 0 & R_{B/\lambda_0}^{\text{aero}} \\ 0 & 0 & -\frac{1}{2}\Omega_{\zeta/\beta_0}\zeta_0 & -\frac{1}{2}\Omega_{\zeta} & 0 & 0 \\ 0 & 0 & [C_{\zeta/\beta_0}^{GB} \quad 0] & [C_{\zeta/\zeta_0}^{GB} \quad 0]\beta_0 & 0 & 0 \\ 0 & F_{2F} & F_{2B} & 0 & 0 & F_3 \end{bmatrix} \quad (47)$$

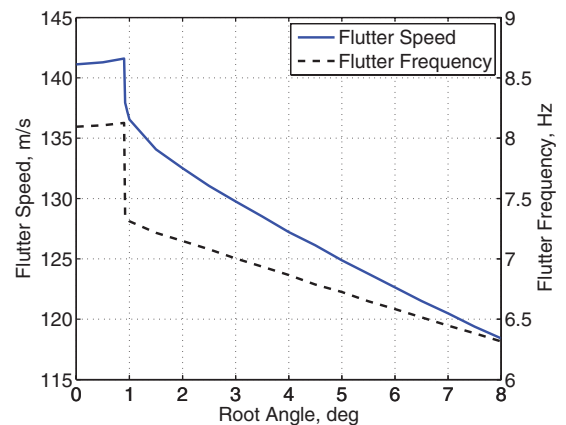


Fig. 7 Flutter speed and frequency at sea level.

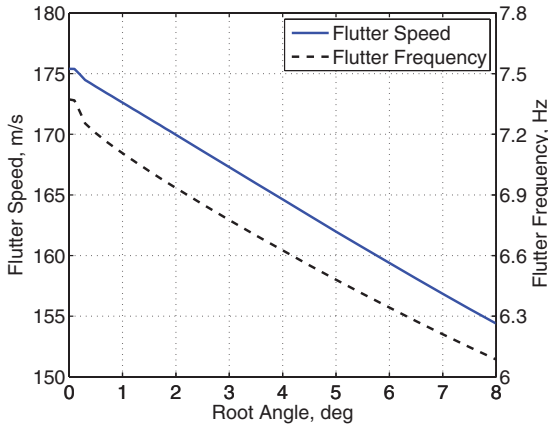


Fig. 8 Flutter speed and frequency at 6096 m altitude.

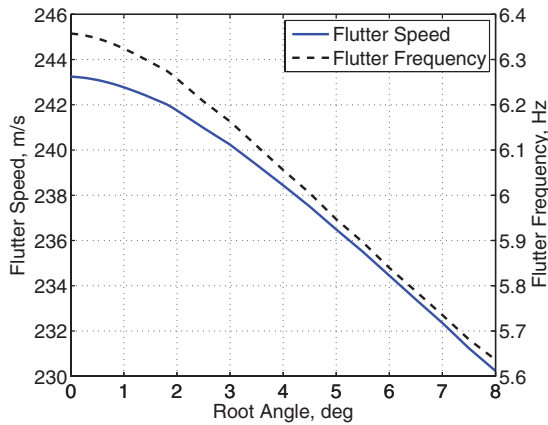


Fig. 9 Flutter speed and frequency at 15,000 m altitude.

G. Solution for the Stability Boundary

The nonlinear stability analysis is conducted in an iterative way, as indicated in Fig. 4. Starting from a predefined flight condition, the system is brought to its trimmed nonlinear steady equilibrium state and linearized about that condition. Eigenvalue analysis of the resulting system matrix \hat{A} in Eq. (44) is performed. The speed is increased and the process is repeated until eigenvalues with positive real parts appear, indicating system instability. One may use the same system matrix for different types of stability analysis, such as flutter of free-flight vehicles, flutter of vehicles with constrained rigid-body motions, or the rigid-vehicle flight dynamic stability. To do so, the

appropriate subset of the system matrix must be defined from Eq. (41).

III. Numerical Studies

A baseline blended-wing-body model is proposed for this study. The wing and body properties are modified from the wall-mounted half-vehicle wind-tunnel model described in [8]. In addition to the half-vehicle model, a full vehicle is also considered. This was created by symmetrically extending the half-vehicle model. Basic physical parameters of the models are given in Table 1.

A. Geometry

Figure 5 shows the geometry of the blended-wing-body model. Both the body and the wings are modeled as beams coupled with aerodynamics. The dashed-dotted line indicates the location of the beam reference axis. The shear center of the beam varies from the body’s root (64.38% of the chord) to the wing root (45.60% of the chord) and keeps its relative position unchanged along the wing. One concentrated mass of 80 kg is positioned at the center of the model, 0.89 m ahead of the reference line. In addition, nine nonstructural masses, 2 kg each, are evenly distributed along the wing from the root to the tip. Each of the wings contains three independent elevons, as indicated in Fig. 5. These elevons occupy 25% of the chord, running from the wing root to 75% of the wing span.

B. System Modes and Frequencies

To assess the vehicle’s flight characteristic, the full aeroelastic/flight dynamic equations of motion are linearized at different trimmed flight conditions. Longitudinal flight modes of the vehicle are then evaluated using the corresponding linearized equations. Figure 6 shows the root loci of these longitudinal modes at different altitudes and flight speeds. It can be seen that both the phugoid and short-period modes are stable in the evaluated range (0–15,000 m and Mach 0.2–0.7). The root locus of the phugoid mode has the tendency to cross the imaginary axis with the increase of Mach number, while its frequency is reduced. On the contrary, the root locus of the short-period mode extends away from both the real and imaginary axes when the speed is increased. At a given speed (say, Mach 0.4, noted by circles in the figure), the damping of the phugoid mode negatively increases with altitude, which indicates a larger stability margin. However, this trend for the short-period mode is reversed.

Table 2 lists the first few fundamental modes of the elastic vehicle. Combining that with Fig. 6, one can see that the frequency of the first flatwise bending mode is right within the variation range of the short-period mode, which means a coupling of these two modes is possible.

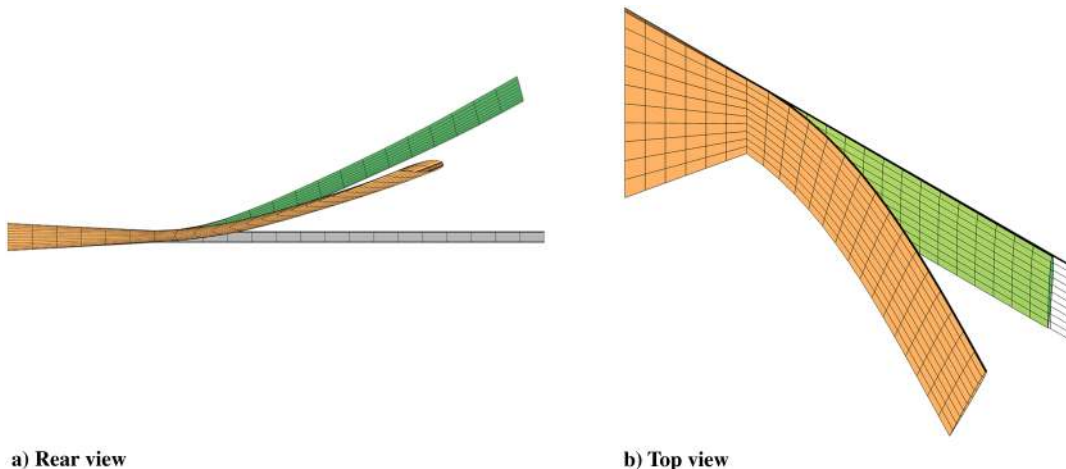


Fig. 10 Flutter mode shapes at sea level (green: zero root angle, orange: 2° root angle).

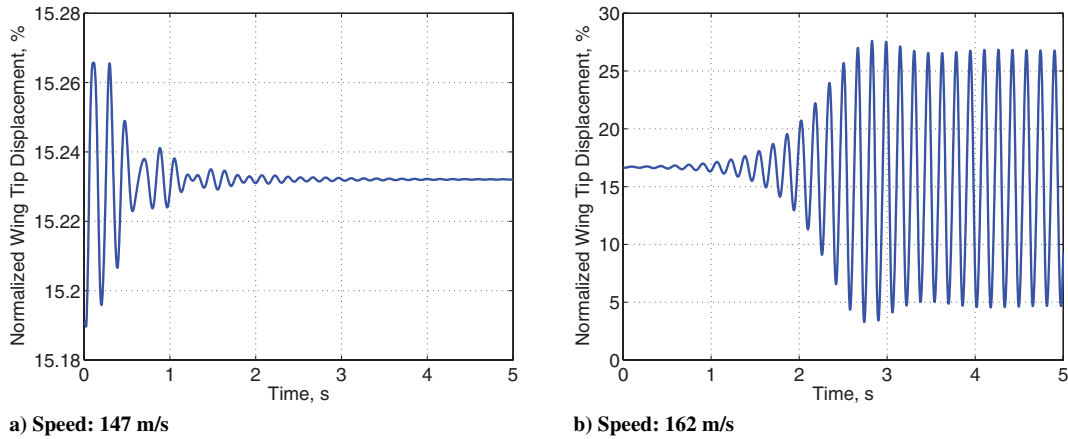


Fig. 11 Normalized wing tip displacements at 6096 m altitude and 8° root angle.

Table 3 Flutter boundaries for different rigid-body motion constraints

Case	Constraint	Speed, m/s	Frequency, Hz
1	Fully constrained	172.52	7.30
2	Free plunging only	164.17	7.07
3	Free pitching/plunging	123.17	3.32
4	Free flight	123.20	3.32

C. Flutter Boundary of Cantilevered Half-Vehicle Model

In this analysis, aeroelastic instabilities of the blended-wing-body aircraft are to be identified over a range of flight conditions, using the proposed process described in Fig. 4. The body angle of a half-vehicle model is varied from 0 to 8 deg, without elevon deflections. However, the rigid-body degrees of freedom are all constrained. This setup simulates the basic test setup in the wind tunnel. The simulation also considers different altitudes (from sea level to 15,000 m). Results obtained are summarized in Figs. 7–9.

By observing the plots of flutter boundaries (Figs. 7–9), one may find different trends at different altitudes. At sea level, the flutter speed is initially slightly increased when the root angle is increased. When a critical value of the angle (about 0.92°) is reached, the flutter boundary is significantly reduced with the increase of the root angle. The discontinuity in the flutter boundary is resulted from a change of flutter modes, similar to what was described in [2]. When the root angle is low, the flutter mode is basically an elastic two-degree-of-freedom flutter: coupled flatwise bending and torsion of the wing. However, when the root angle is larger than the critical value, the in-plane bending participates in the unstable mode, as shown in Fig. 10, resulting in a three-degree-of-freedom flutter. At the higher altitudes (6096 and 15,000 m), the flutter speed decreases with the increase of

the root angle and the flutter mode is always a three-degree-of-freedom one: coupled flatwise bending, in-plane bending, and torsion of the wing, although the contribution of the in-plane bending to the flutter mode is very small when the root angle is about zero. With higher root angles, the increased wing flatwise bending curvature due to larger aerodynamic loads facilitates the coupling between the in-plane bending and torsion modes [2], making the in-plane bending contribution more significant.

To verify the nonlinear flutter boundary calculation presented above, two individual nonlinear time-domain simulations are performed. With the altitude of 6096 m and the root angle of 8°, one of the simulations has a flow velocity (147 m/s) under the flutter speed (154.39 m/s), while the other does at a slightly higher flow velocity (162 m/s) than the flutter speed. The time histories of the tip displacements (normalized with respect to the half-vehicle span) are plotted in Fig. 11. From Fig. 11a, the wing deformation of the preflutter case is stabilized after some initial oscillations. However, the wing oscillation is self-excited for the postflutter case, as seen from Fig. 11b. The amplitude of the wing oscillation is increased, until it reaches a limit cycle oscillation.

D. Flutter Boundary of Full Vehicle in Flight

As it has been discussed, the wings of this vehicle are flexible in such a way that their elastic modes are coupled with the rigid-body modes of the whole vehicle. Therefore, the evaluation of the stability of the full vehicle should include the rigid-body degrees of freedom, which gives the stability boundary in free flight.

As an example, the full-vehicle stability is evaluated at 6096 m altitude for the level flight condition, i.e., the vehicle is trimmed for every flight speed at which the stability is evaluated. To assess the coupling between the wing elastic deformation and the rigid-body motion, multiple constraints to the rigid-body degrees of freedom are

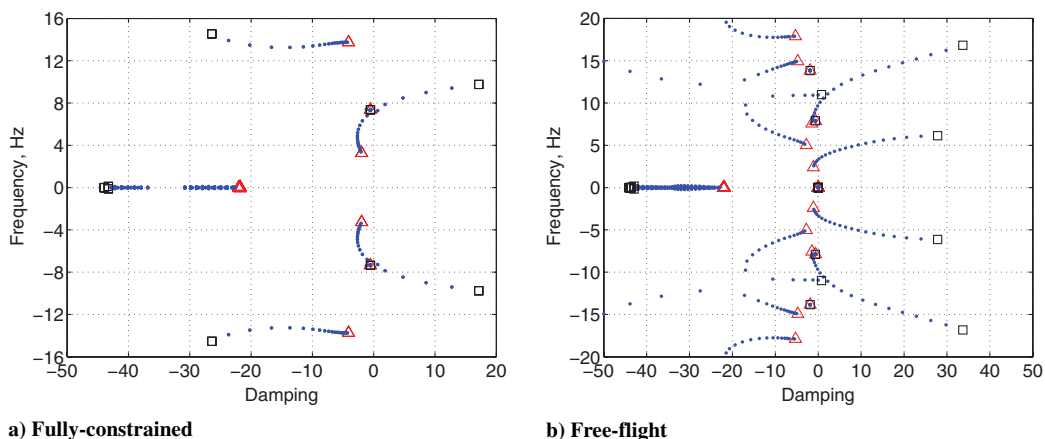


Fig. 12 Aeroelastic root locus of the blended-wing-body configuration at 6096 m altitude; speed from 100 m/s (triangle) to 200 m/s (square).

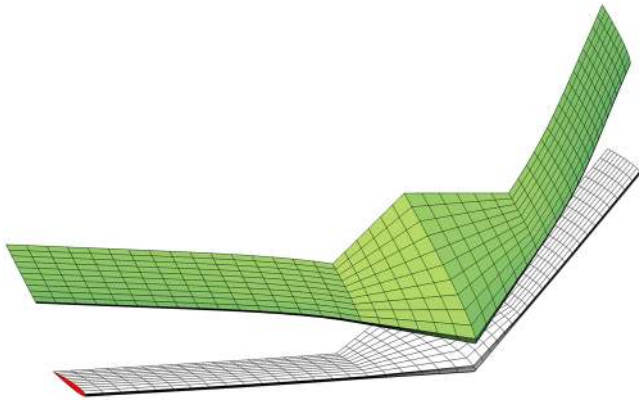


Fig. 13 Flutter mode shape of the free-flight case at 6096 m altitude.

used in the calculation of the flutter boundary. First, the vehicle has all rigid-body motions constrained (case 1). Then, the plunging motion is set free (case 2), followed by another case with both plunging and pitching set free (case 3). Finally, all rigid-body degrees of freedom are free and allowed to couple with the wing deformations (case 4).

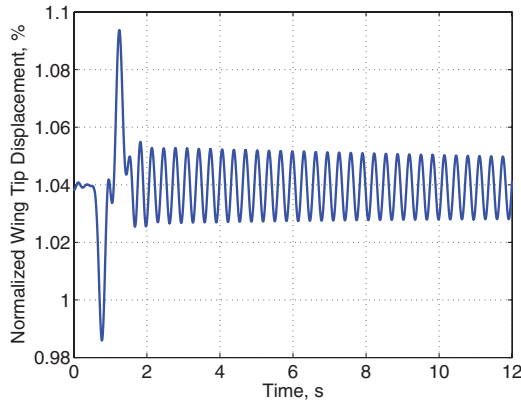
The flutter speed and frequency corresponding to each of the four different cases are listed in Table 3. These results are obtained using the proposed process described in Fig. 4. The root loci of cases 1 and 4 are plotted in Fig. 12. Figure 13 illustrates the flutter mode shape of case 4, with the vehicle in wire frame as the reference shape and position. From this figure, one may find that the rigid-body mode is a coupled pitching/plunging compared to the reference, while the wing

elastic mode consists of both flatwise bending and twist. The swept-wing platform favors the coupling between the pitching/plunging of the rigid body and the bending/twist of the wings. Since the rigid-body components of the unstable mode for case 4 consist only of the pitching and plunging motions, the flutter speed of this case is nearly identical to case 3, with only pitching and plunging degrees of freedom. For the case when only plunging is free, there is no coupling between wing deformation and the pitching of the body, which results in a weak coupling between the wing elastic deformation and the free rigid-body motion. That flutter boundary is the closest to the case with the rigid-body degrees of freedom fully constrained.

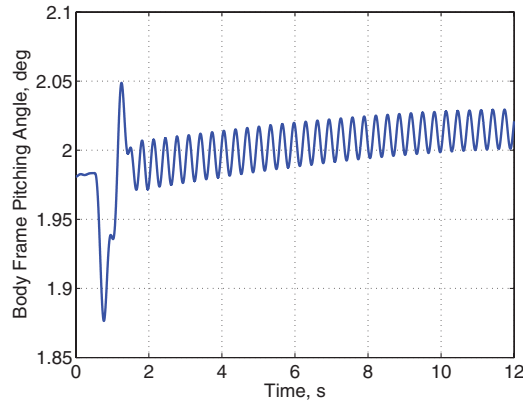
In the time domain, two individual nonlinear simulations are carried out for verification purposes, one of which simulates the level flight of the vehicle with a flight velocity lower than the flutter speed (120 m/s), while the other flies with a slightly higher velocity (125 m/s) than the flutter speed. A sinusoidal deflection of all the three elevons is used as a small perturbation to the system equilibrium. The elevon input is given by

$$\delta = \begin{cases} 0 & t < 0.5 \text{ s} \\ -0.1 \sin 2\pi(t - 0.5) \text{ deg} & 0.5 \text{ s} \leq t \leq 1.5 \text{ s} \\ 0 & t > 1.5 \text{ s} \end{cases} \quad (48)$$

The time histories of the tip displacement and body-frame pitching angle are plotted in Figs. 14 and 15. For the preflutter case (see Fig. 14), the responses converge after initial oscillations. However, the responses of the postflutter case diverge, exhibiting instability, as shown in Fig. 15. As one can see from Fig. 15b, the pitching motion is not stable, which is correctly predicted by the eigenvalue analysis. One more observation from the time-domain simulation is that the

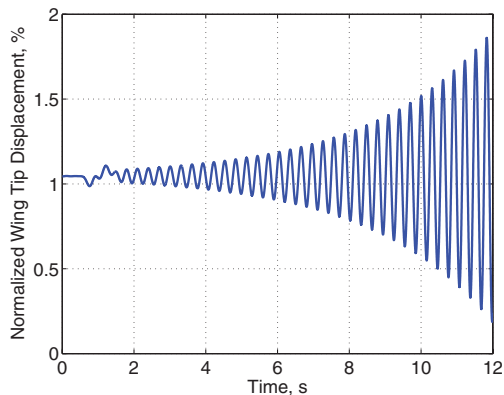


a) Wing tip displacement

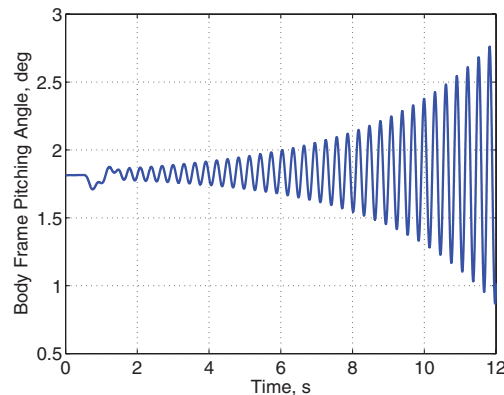


b) Body frame pitching angle

Fig. 14 Normalized wing tip displacement and body-frame pitching angle of the preflutter case for the blended-wing-body vehicle at 6096 m altitude; speed 120 m/s.



a) Wing tip displacement



b) Body frame pitching angle

Fig. 15 Normalized wing tip displacement and body-frame pitching angle of the postflutter case for the blended-wing-body vehicle at 6096 m altitude; speed 125 m/s.

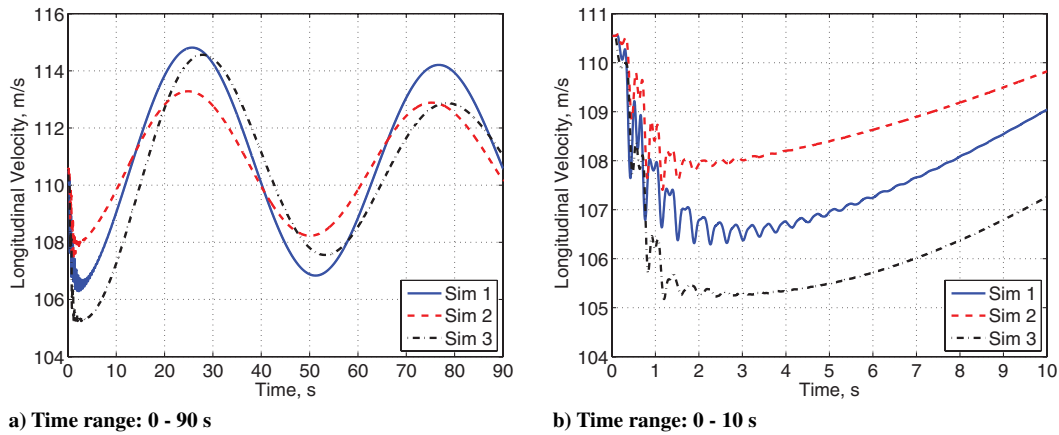


Fig. 16 *B*-frame longitudinal velocity with gust perturbation for different simulations at 6096 m altitude.

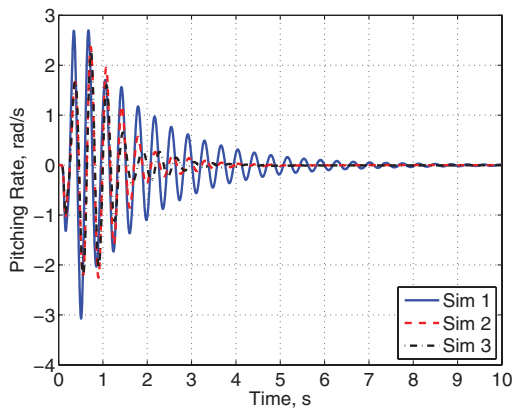


Fig. 17 *B*-frame pitching rate with gust perturbation for different simulations at 6096 m altitude.

frequency of the unstable oscillation is approximately 3.33 Hz, which agrees with the eigenvalue analysis within 0.3%.

E. Response of Full Vehicle to Gust Perturbations

To better understand the nonlinear nature of the aeroelastic stability, the vehicle is simulated under gust perturbations. The simulation is conducted at 6096 m with the flight speed of 110.64 m/s (Mach 0.35). A discrete gust model is used, whose spatial distribution is governed by a 1-cosine function, with the maximum gust speed of 15.24 m/s (50 ft/s) and the gust region along the flight path extending for 13.72 m, which is approximately 25 times the wing chord length. The gust is symmetrically applied to the vehicle. Note

that stall effects are considered through a simplified stall model [5] when the local angle of attack at an airfoil reaches the critical stall angle.

There are three types of simulation considered: 1) nonlinear simulation with follower aerodynamic loads (sim 1), 2) linearized simulation with follower aerodynamic loads (sim 2), and 3) linearized simulation with fixed-direction aerodynamic loads (sim 3). The simulation results are compared in Figs. 16–20. It can be seen that the applied gust perturbation does not excite any instability of the vehicle. The phugoid mode can be clearly observed from the plots of longitudinal velocity (Fig. 16) and altitude (Fig. 19). This mode is stable and slightly damped. One may measure the period of the phugoid mode, and only the period from nonlinear simulation with follower aerodynamic loads (sim 1) agrees with what has been predicted from the eigenvalue analysis (see Fig. 6). The other two simulations give results that are slightly off, with significant difference in oscillation amplitudes. For the linearized simulation with fixed-direction aerodynamic loads (the dashed-dotted line in Fig. 19), the vehicle altitude is not recovered after one cycle. Therefore, it does not accurately simulate the phugoid motion.

The high-frequency response at the initial stages is associated with the short-period mode excited by the gust perturbation. The amplitude of this oscillation decays quickly with a high negative damping. One may find that the short-period mode frequency (Figs. 17 and 18) is quite close to that of the wing elastic oscillation (Fig. 20), which indicates coupling between the two motions.

To study the effects of the gust on the vehicle response at subcritical conditions, the flight speed of the vehicle is increased to 122 m/s, which is approximately 1% lower than the flutter boundary. The same nominal gust is used for the nonlinear simulation with follower aerodynamic loading. The results are compared with another simulation, in which the vehicle flies in calm air (see Figs. 21–26). One may find that the flight in calm air is stable, as the

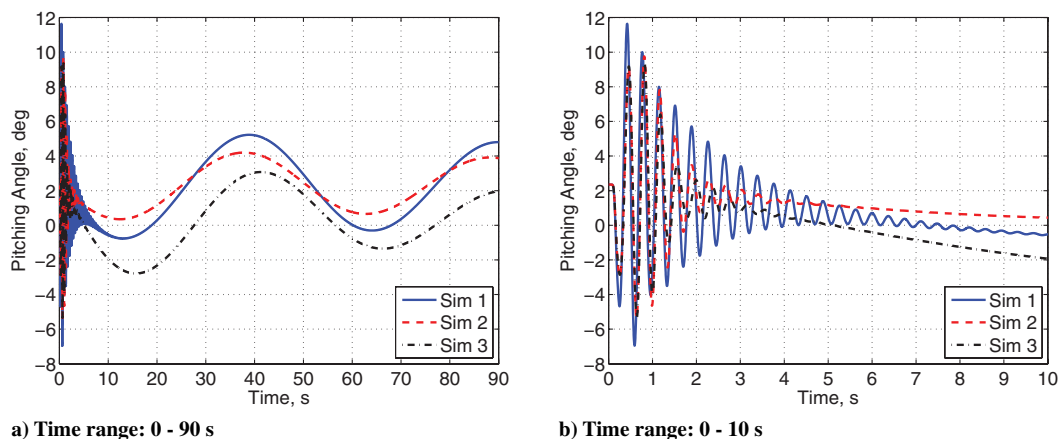
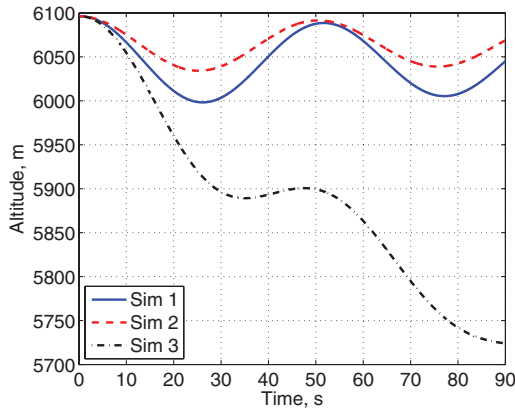
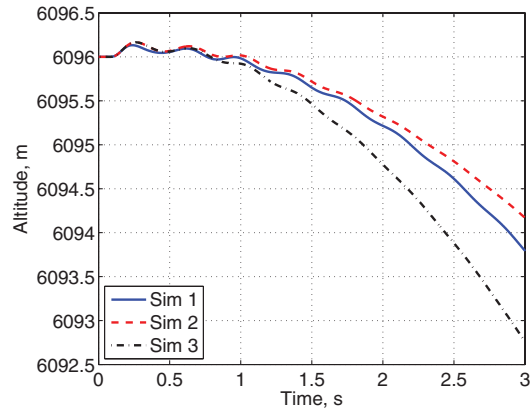


Fig. 18 *B*-frame pitching angle with gust perturbation for different simulations at 6096 m altitude.



a) Time range: 0 - 90 s



b) Time range: 0 - 3 s

Fig. 19 Altitude change with gust perturbation for different simulations at 6096 m altitude.

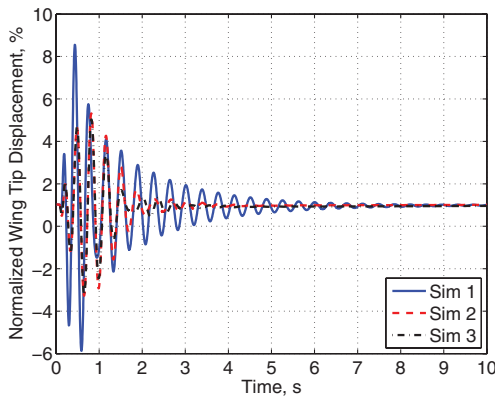


Fig. 20 Normalized wing tip displacement (with respect to the half-vehicle span) with gust perturbation for different simulations at 6096 m altitude.

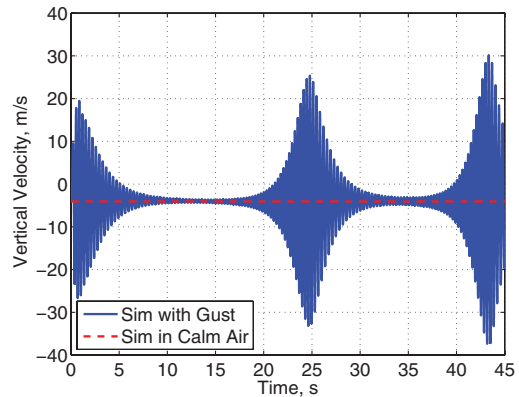


Fig. 22 B frame vertical velocity with gust perturbation at the subcritical condition; altitude 6096 m.

speed is lower than the flutter boundary. However, the finite gust perturbation brings instability to the whole system even after the perturbation is over. The vehicle sinks due to the gust perturbation and the flight velocity is increased to be greater than the flutter boundary after 15 s, where the short-period mode coupled with the wing elastic bending deformation grows to be unstable. Eventually, this motion develops into a beating oscillation (see Figs. 23, 24, and 26).

F. Aeroelastic Tailoring

In the nominal blended-wing-body model, there is no elastic coupling in the stiffness matrix between the torsion and the out-of-

plane bending of the wing. A tuning parameter σ is used for the tailoring of the wing stiffness, such that the cross-sectional torsion/out-of-plane bending coupling stiffness k_{23} is determined by

$$k_{23} = \sigma \sqrt{k_{22} \cdot k_{33}} \quad \sigma = 0, \pm 0.25, \pm 0.50, \pm 0.75 \quad (49)$$

The change of torsion/out-of-plane bending coupling may impact the vehicle's stability boundary. To evaluate the impact, the flutter boundary of the vehicle in free-flight condition (level flight at 6096 m altitude, no constraints in rigid-body degrees of freedom) is calculated for configurations with different coupling levels. The variation of the flutter boundary is plotted in Fig. 27. By looking at the unstable mode shapes for these configurations, one may find that

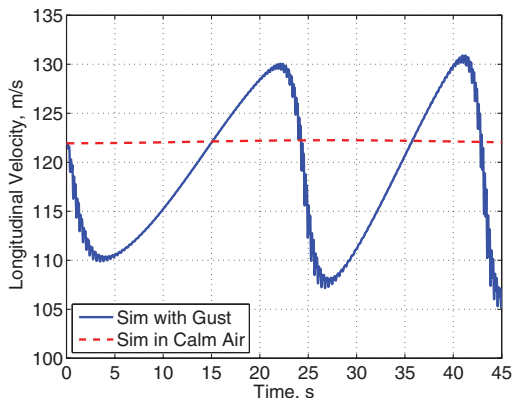


Fig. 21 B frame longitudinal velocity with gust perturbation at the subcritical condition; altitude 6096 m.

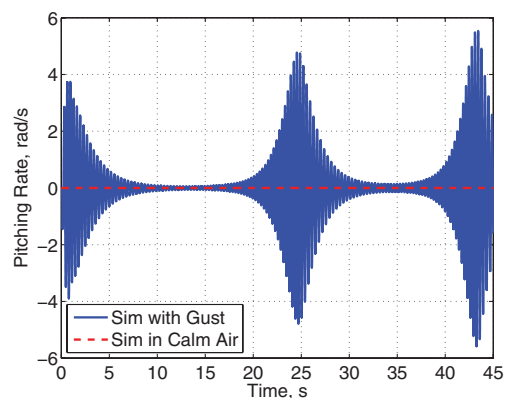


Fig. 23 B frame pitching rate with gust perturbation at the subcritical condition; altitude 6096 m.

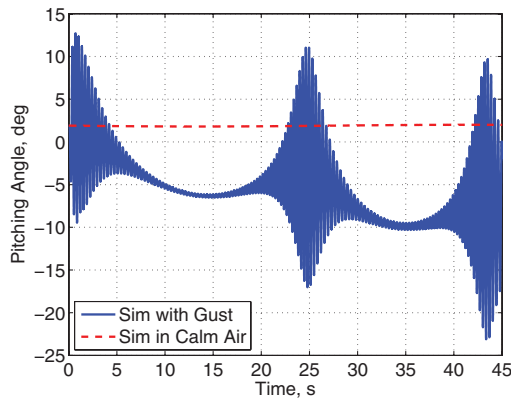


Fig. 24 B frame pitching angle with gust perturbation at the subcritical condition; altitude 6096 m.

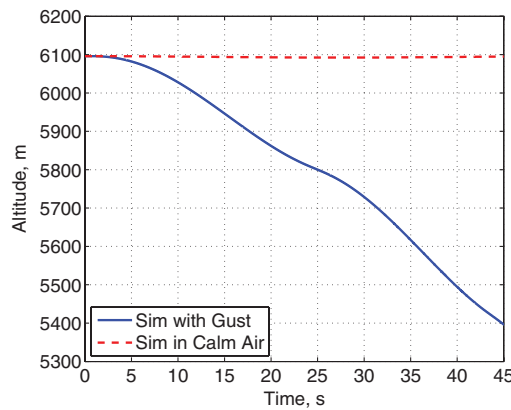


Fig. 25 Altitude change with gust perturbation at the subcritical condition; altitude 6096 m.

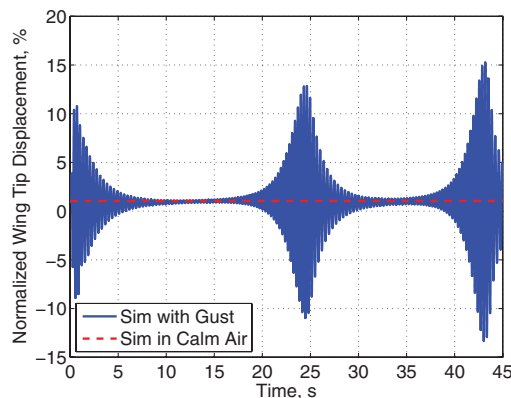


Fig. 26 Normalized wing tip displacement (with respect to the half-vehicle span) with gust perturbation at the subcritical condition; altitude 6096 m.

the shift of flutter mode when the tuning parameter is changed from positive to negative. If the coupling between the torsion and out-of-plane bending stiffness is positive, the flutter modes are the same as the nominal configuration, as shown in Fig. 13. However, if the coupling is negative, the flutter modes are switched to the roll motion of the body with complex in-plane/out-of-plane bending and twist of the wing, as described in Fig. 28. It is also noticeable that the flutter boundary is more sensitive to the positive coupling coefficient (wash in) than the negative one (wash out). When the tuning parameter is +0.75, the flutter speed is reduced to less than half of the nominal configuration. Also, no higher flutter speed was found than the one with σ equal to zero.

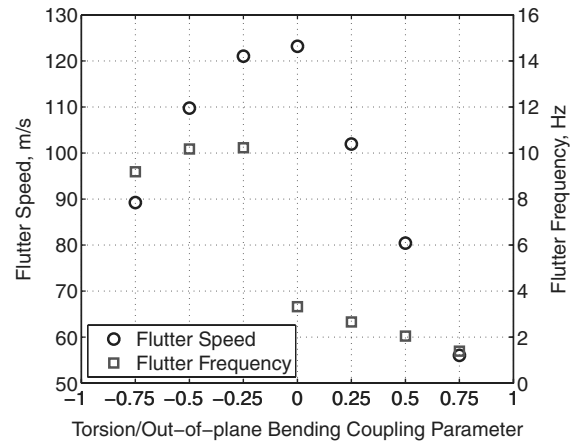


Fig. 27 Change of flutter speed and frequency in free flight with different torsion/out-of-plane bending elastic coupling effects.

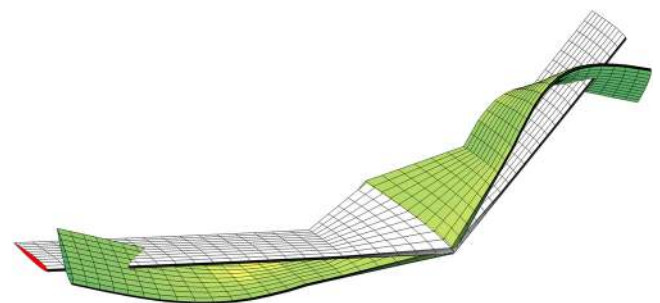


Fig. 28 Antisymmetric mode shape with -0.75 coupling parameter.

IV. Conclusions

In this paper, the coupled nonlinear flight dynamic and aeroelastic stability characteristics of a blended-wing-body aircraft were described by a set of nonlinear equations. The geometrically nonlinear structural analysis was performed using a strain-based formulation, which was able to capture the large deformations in slender structures effectively. Finite state unsteady subsonic aerodynamic loads were coupled with the structural formulation, which completed the aeroelastic formulation. Nonlinear equations of motion for a frame attached to the vehicle (not necessarily at its c.g. point) were used to complete the coupled flight dynamic/aeroelastic formulation. With these equations, fully nonlinear time-marching analyses were performed. The nonlinear equations were also linearized about a given nonlinear state and put into the state-space form, such that stability boundary and flight dynamic modes could be assessed.

Longitudinal flight dynamic modes were studied for a sample model vehicle with the Mach number ranging from 0.2 to 0.7 at different altitudes. In the studied range, the phugoid and short-period modes of this vehicle were both stable. However, the frequency of the elastic wing-body bending mode was low enough that it could couple with the short-period mode of the rigid body. That means the rigid-body motion could excite the instability of the wing-body elastic system, which introduces a special type of dynamic instability: body-freedom flutter.

Enlightened by the above analyses, the flutter boundary of the whole vehicle was studied with different rigid-body constraints. For the particular vehicle studied here, the body-freedom flutter was the result of the coupled short-period mode with the wing elastic bending/torsion mode. As the wing oscillations were coupled with the rigid-body motion of the entire vehicle, the flutter boundary in free-flight condition differed from that of a constrained vehicle. Both the flutter boundary and the unstable modes obtained in free flight

were different from the one in wind-tunnel tests when the rigid-body motions were fully constrained. This indicated that for the vehicles with very flexible wing members, the flutter analysis should consider the whole vehicle's degrees of freedom, including the rigid-body modes. The traditional method of performing wind-tunnel tests in a constrained model to evaluate its flutter boundary may not be appropriate.

To study the gust response, a spatially distributed discrete gust model was seamlessly incorporated into the time simulation scheme. The gust perturbation was symmetrically applied to the vehicle. Three types of simulations were performed: 1) nonlinear simulation with follower aerodynamic loads, 2) linearized simulation with follower aerodynamic loads, and 3) linearized simulation with fixed-direction aerodynamic loads. Only the nonlinear simulation with follower aerodynamic loads could accurately simulate the phugoid mode predicted in the eigenvalue analysis. Moreover, the phugoid mode was not observed from the simulation with fixed-direction aerodynamic loads. This indicated the importance of the nonlinear analysis to the flight dynamic responses, especially the follower nature of the aerodynamics, even though the overall elastic deformation of the wings was small. The finite gust perturbation could bring instability to the vehicle at subcritical flight conditions. As the simulation performed in this study was only open-loop, future efforts can be made to design an appropriate control schemes to alleviate the instability under finite gust perturbations.

Finally, the nominal configuration was elastically tailored with different levels of bending/twist elastic coupling stiffness of the wings. For the example configuration, both the positive and negative couplings resulted in reduction of the flutter boundary. However, the negative coupling introduced a different antisymmetric flutter mode.

Acknowledgments

This work was supported in part by the U.S. Air Force Research Laboratory (AFRL) under the Michigan/AFRL Collaborative Center in Aeronautical Sciences (MACCAS), with Gregory Brooks as the task Technical Monitor.

References

- [1] Van Shoor, M. C., Zerweck, S. H., and von Flotow, A. H., "Aeroelastic Stability and Control of a Highly Flexible Aircraft," 30th AIAA/ASME/ASCE/AHS/ASC Structures, Structural Dynamics and Materials Conference, Mobile, AL, AIAA Paper 1989-1187, Apr. 1989.
- [2] Patil, M. J., Hodges, D. H., and Cesnik, C. E. S., "Nonlinear Aeroelasticity and Flight Dynamics of High-Altitude Long-Endurance Aircraft," *Journal of Aircraft*, Vol. 38, No. 1, 2001, pp. 88–94. doi:10.2514/2.2738
- [3] Drela, M., "Integrated Simulation Model for Preliminary Aerodynamic, Structural, and Control-Law Design of Aircraft," 40th AIAA/ASME/ASCE/AHS/ASC Structures, Structural Dynamics, and Materials Conference and Exhibit, St. Louis, MO, AIAA Paper 1999-1394, Apr. 1999.
- [4] Shearer, C. M., and Cesnik, C. E. S., "Nonlinear Flight Dynamics of Very Flexible Aircraft," *Journal of Aircraft*, Vol. 44, No. 5, 2007, pp. 1528–1545. doi:10.2514/1.27606
- [5] Su, W., and Cesnik, C. E. S., "Dynamic Response of Highly Flexible Flying Wings," 47th AIAA/ASME/ASCE/AHS/ASC Structures, Structural Dynamics, and Materials Conference, Newport, RI, AIAA Paper 2006-1636, May 2006.
- [6] Tilmann, C. P., Flick, P. M., Martin, C. A., and Love, M. H., "High-Altitude Long Endurance Technologies for SensorCraft," RTO AVT Symposium on Novel and Emerging Vehicle and Vehicle Technology Concepts (AVT-099), Brussels, Research and Technology Organisation Paper MP-104-P-26, Apr. 2003.
- [7] Beran, P. S., Hur, J. Y., Snyder, R. D., Strong, D., Bryson, D., and Strganac, T., "Static Nonlinear Aeroelastic Analysis of a Blended Wing Body," 46th AIAA/ASME/ASCE/AHS/ASC Structures, Structural Dynamics, and Materials Conference, Austin, TX, AIAA Paper 2005-1994, Apr. 2005.
- [8] Lockyer, A. J., Drake, A., Bartley-Cho, J., Vartio, E., Solomon, D., and Shimko, T., "High Lift over Drag Active (HiLDA) Wing," Northrop Grumman Corp., Rept. AFRL-VA-WP-TR 2005-3066, El Segundo, CA, Apr. 2005.
- [9] Livne, E., and Weisshaar, T. A., "Aeroelasticity of Nonconventional Airplane Configurations—Past and Future," *Journal of Aircraft*, Vol. 40, No. 6, 2003, pp. 1047–1065. doi:10.2514/2.7217
- [10] Love, M. H., Zink, P. S., Wieselmann, P. A., and Youngren, H., "Body Freedom Flutter of High Aspect Ratio Flying Wings," 46th AIAA/ASME/ASCE/AHS/ASC Structures, Structural Dynamics, and Materials Conference, Austin, TX, AIAA Paper 2005-1947, Apr. 2005.
- [11] Cesnik, C. E. S., and Brown, E. L., "Modeling of High Aspect Ratio Active Flexible Wings for Roll Control," 43rd AIAA/ASME/ASCE/AHS/ASC Structures, Structural Dynamics, and Materials Conference, Denver, CO, AIAA Paper 2002-1719, Apr. 2002.
- [12] Cesnik, C. E. S., and Brown, E. L., "Active Wing Warping Control of a Joined-Wing Airplane Configuration," 44th AIAA/ASME/ASCE/AHS/ASC Structures, Structural Dynamics, and Materials Conference, Norfolk, VA, AIAA Paper 2003-1715, Apr. 2003.
- [13] Cesnik, C. E. S., and Su, W., "Nonlinear Aeroelastic Modeling and Analysis of Fully Flexible Aircraft," 46th AIAA/ASME/ASCE/AHS/ASC Structures, Structural Dynamics, and Materials Conference, Austin, TX, AIAA Paper 2005-2169, Apr. 2005.
- [14] Peters, D. A., and Johnson, M. J., "Finite-State Airloads for Deformable Airfoils on Fixed and Rotating Wings," *Symposium on Aeroelasticity and Fluid/Structure Interaction, ASME Winter Annual Meeting*, edited by P. P. Friedmann and J. C. I. Chang, American Society of Mechanical Engineers, New York, Nov. 1994, pp. 1–28.
- [15] Peters, D. A., Karunamoorthy, S., and Cao, W.-M., "Finite State Induced Flow Models Part I: Two-Dimensional Thin Airfoil," *Journal of Aircraft*, Vol. 32, No. 2, 1995, pp. 313–322. doi:10.2514/3.46718